Extreme isotopic variation documents extensional tectonics in arc magmas from Methana, Greece.

M.A. Elburg[1,2], I. Smet[2], P. Van den haute[2], F. Vanhaecke[3], M. Klaver[4,5], T. Andersen[1,6]

[1] Department of Geology, University of Johannesburg, PO Box 524, Auckland Park 2006, South Africa marlinae@uj.ac.za

[2] Department of Geology, Ghent University, Krijgslaan 281 – S8, BE9000 Gent, Belgium

[3] Department of Analytical Chemistry, Ghent University, Krijgslaan 281 – S12, BE9000 Gent, Belgium

[4] Department of Geology and Geochemistry, Vrije Universiteit, De Boelelaan 1085, 1081 HV Amsterdam, The Netherlands

[5] School of Earth Sciences, University of Bristol, Wills Memorial Building, Queen's Road, Bristol BS8 1RJ, United Kingdom

[6] Department of Geosciences, University of Oslo, PO Box 1047 Blindern, N-0316, Norway

Key words: subduction, Aegean Arc, crustal contamination, radiogenic isotopes, extension

Highlights:

- Volcanic products from Methana (Greece) show large isotopic variation
- Isotopic signature and eruption style document tectonic regime
- Greatest isotopic variation and explosive deposits during extension
- Magma mixing responsible for isotopic arrays

Abstract

New Sr-Nd-Hf-Pb isotope data for volcanic rocks from the peninsula of Methana (South Aegean Active Volcanic Arc, Greece) show a wide variation, and more 'enriched' isotopic signatures (e.g. elevated $^{87}Sr/^{86}Sr$ at 0.705-0.709) than those of other active Aegean volcanic centres, all located on thinner crust. The data set is best explained by polybaric AFC processes, with contaminants similar to country rocks and xenoliths, showing moderately high $^{87}Sr/^{86}Sr$ ratios, and with isotopically more evolved lower crust, similar to the pre-Alpine Ios basement. Pb isotope ratios show some minor influence of assimilation of fluid-altered volcanic cumulates. Intermediate lava domes with mafic enclaves were formed during periods of compression, whereas an extensional period saw the deposition of explosive products of bimodal composition, with the more felsic deposits showing the most pronounced influence of crustal assimilation. The latter likely represent stalled magmas from an earlier compressional period, which were remobilised and flushed out by ascending mafic magmas during extension. Recognition of these volcanological, geochemical and isotopic characteristics of deposits associated with

extensional tectonics in a modern arc will enable us to use these criteria to infer paleo-tectonics from older volcanic deposits.

1. Introduction

The role of regional tectonics in the style of volcanism and the composition of the erupted products at convergent plate margins has been increasingly recognised in recent years (Defant, 1992; Elburg et al., 2004; Shinjo, 1999; Straub and Zellmer, 2012; Zellmer, 2009). The effects are most noticeable in complicated convergent settings, such as near-collisional situations, where the arrival of small continental fragments at the trench influences the stress regime of the arc as whole. The Aegean arc is such a system, and for this study we concentrate on the volcanic peninsula of Methana (Greece; Fig. 1). Methana is a nominally active volcano in the westernmost part of the South Aegean Volcanic Arc, with a magmatic record extending from the mid-Pliocene to 230 BC (Pe-Piper and Piper, 2013). It is a typical continental arc volcano, consisting of mainly intermediate to felsic lava domes and minor explosive magmatic deposits, emplaced upon a basement that consists of Mesozoic limestones, with minor siliciclastic and mélange-type rocks (Dietrich and Gaitanakis, 1995). Since the reconnaissance-style analyses of Sr isotope ratios of the lavas that were performed during the 1970's (Pe-Piper, 1975), it has been known that the magmatic system of Methana has seen a greater influence of crustal materials than the presently active Aegean volcanoes of Santorini and Nisyros, and this has been confirmed by more recent data (e.g. Elburg et al., 2014; Woelki et al., 2018). The style of magmatic activity on Methana, and the eruption rates, have been argued to have been strongly influenced by regional tectonics (Pe-Piper and Piper, 2013). This also affected the major and trace element geochemistry of the erupted products. For instance, the most primitive magmas erupted during a period of strike-slip faulting

that provided crustal-scale pathways for magma transport to the surface (Pe-Piper and Piper, 2013). In this scenario, the magmas erupted during this strike-slip event would also be the least contaminated, as they would have had less opportunity to interact with the country rocks. This idea, however, has not been tested with systematic isotopic investigations, and the present paper will redress this omission.

The obtained whole rock major and trace element and Sr-Nd-Hf-Pb isotopic data for the various igneous units, including their mafic enclaves, as well as country rocks and xenoliths, will be used to assess the identity of potential assimilants, and the processes that led to the wide range of geochemical and isotopic variation observed in the volcanic products of Methana volcano. We will show that the wide geochemical variation is dominantly a result of assimilation of a variety of crustal rocks, with the most extensive range seen in the explosive deposits that surfaced during a period of extensional tectonics.

2. Geological setting

The South Aegean Active Volcanic Arc is the present-day manifestation of the long-lived convergence system between Africa and Europe, which has been active since the Jurassic (Van Hinsbergen et al., 2005). Convergence between the two continents has been accommodated by subduction, nappe stacking and periodic back-stepping of the volcanic arc, which resulted in the present-day volcanic arc being located on continental crust that originated from the East-African (Keay and Lister, 2002; Van Hinsbergen et al., 2005) and ‘Amazonian’ (South American: Zlatkin et al., 2014) cratons. Slab roll-back in a southward direction has been ongoing since the Oligocene and was responsible for the formation of the Aegean Sea (Jolivet et al., 2015).

The active South Aegean Volcanic Arc extends from the Saronic Gulf centres of Methana and Aegina in the west, through Milos and Santorini to Yali-Nisyros in the east (Fig. 1a). On the Greek mainland, west of the Saronic Gulf, the Crommyonia volcanic centres were active around 4 and 2.5 Ma. The volcanic centre of Methana is situated on the Pelagonian Unit (Pe-Piper and Piper, 2002) that forms the upper nappe of the Internal Hellenides, of which the exposed rocks are dominated by Mesozoic limestones, and which is thought to be underlain by the pre-Alpine (perhaps even pre-Variscan) basement of the Cycladic Blueschist Unit, as exposed on, for instance, Ios and Sikinos (Mizera and Behrmann, 2015). The area was already part of a magmatic arc during the Miocene, and granitoids with ages between 11 and 17 Ma (Bolhar et al., 2010) are common on the Cycladic islands (e.g. Naxos) and mainland Greece (e.g. Laurion). They are likely also present in the basement underlying the present-day volcanic arc (e.g. Skarpelis and Kyriakopoulos, 1992). The thickness of the crust under the Saronic Gulf has been estimated to be 30 km based on the tomographic work of Karagianni et al. (2005), which is thicker than underneath the other Aegean volcanic centres such as Santorini (20 km) and Nisyros (25 km).

The tectonic evolution of the Saronic Gulf has been summarized most recently by Pe-Piper and Piper (2013), who also presented absolute and relative ages for the different volcanic units on the peninsula. They defined three main periods in the tectonic evolution of Methana, whereby the first period (around 3.5 Ma) saw the emplacement of volcanic domes along N-S faults (volcanic phase A; Fig. 1b). These oldest volcanic deposits were partially eroded to yield the volcaniclastic ‘apron’ assigned to Phase B. Volcanic phases C to E (early-middle Pleistocene, ca. 1.5-0.5 Ma) coincided with enhanced uplift and active NE-SW strike-slip faulting. Uplift accelerated around 0.38 Ma, giving rise to steep normal faults, and associated

122 voluminous eruptions of volcanic phase F and G. Volcanic phase H, comprising the
123 most recent, historic activity, occurred during the waning stages of this regime.

124

125 **3. Analytical techniques**

126 A detailed description of the analytical techniques is given in supplementary material
127 S1, which also gives data on international standards.

128 All analyses were performed on agate-milled samples, with major elements being
129 determined by ICP-OES after Li-borate fusion-assisted dissolution, and trace
130 elements by ICP-MS after HF-HNO_3 dissolution in capped teflon vials. Reported Zr
131 concentrations are from ICP-OES analyses, as only the flux-assisted dissolution
132 procedure assures that all zircon is dissolved. Sr, Nd and Pb isotopic measurements
133 were performed, using a Thermo-Scientific Neptune at Ghent University, on the same
134 splits as those used for preparing the solutions for trace element analysis, after
135 isolation of the elements of interest. Hf isotopes were measured using a Thermo-
136 Scientific Neptune at the Vrije Universiteit Amsterdam on low- and high-pressure (for
137 zircon-bearing samples) dissolutions, after isolation of Hf from its matrix. During the
138 course of the analyses, international standards gave results within the uncertainty of
139 their accepted values (e.g. BHVO-2 (± 2SD): $^{87}Sr/^{86}Sr$ = 0.705020 ± 0.000013;
140 $^{143}Nd/^{144}Nd$ = 0.512975 ± 0.000024; $^{176}Hf/^{177}Hf$ = 0.283096 ± 0.000018; JB-2:
141 $^{206}Pb/^{204}Pb$ = 18.345 ± 0.01, $^{207}Pb/^{204}Pb$ = 15.564 ± 0.01, $^{208}Pb/^{204}Pb$ = 38.287 ± 0.02)

142 Zircons were separated using heavy liquids and, after cathodoluminescence imaging,
143 analysed for their Hf isotope ratios by LA-MC-ICPMS (Nu Plasma combined with
144 NWR-213 ablation system) at the Department of Geosciences of the University of
145 Oslo, following the procedures described by Elburg et al. (2013). A few spots were
146 ablated for U-Pb dating with the same set-up to see whether a numerical age could

147 be determined with the set-up used. The results indicated that the age was < 5 Ma,
148 but no attempt at further quantification was made because of the lack of suitable
149 standards.

150

151 **4. Distribution and petrography of volcanic rocks**

152 We follow the newly established volcanic stratigraphy from Pe-Piper and Piper (2013)
153 for the description and interpretation of our data, ranging from the domes of Phase A
154 at the base (ca. 3.5 Ma) through to the historic eruption of Phase H at Mavri Petra.
155 Sample locations are given in Fig. 1b, and in supplementary material S2. Apart from
156 the igneous rocks, samples of country rocks and xenoliths were also obtained to
157 assess their role as crustal contaminants. Apart from Phase C, which also hosts
158 explosive deposits, all volcanic phases are dominated by effusive volcanic products.
159 In our description below, we first focus on the effusive deposits, and then on the
160 Phase C deposits.

161 The effusive deposits occur mainly in the shape of lava domes and flows. Mafic
162 enclaves are common (Fig. 2a,b), although their volume percentage, shapes and
163 sizes are variable. The groundmass of the lavas typically consists of very fine-
164 grained plagioclase, pyroxenes ± hornblende. Most lavas are crystal-rich, with
165 plagioclase (showing polysynthetic twinning, oscillatory zoning and sieve-textured
166 zones) occurring as a common constituent. The lavas are generally hornblende- and
167 sometimes also biotite-bearing, but most deposits also contain lavas that are poor in
168 hydroxyl-bearing minerals. In many samples, the hornblende is partially to wholly
169 replaced by opacite (Fig. 3a), and in the hornblende-poor samples, some larger
170 aggregates can be recognised as pseudomorphs after hornblende or biotite, but they
171 are wholly replaced by hydroxyl-free minerals. Disequilibrium textures are common in

the hornblende-rich rocks: resorbed quartz crystals can be observed occasionally mantled by small clinopyroxene crystals and occurring in the same sample as olivine crystals, olivine crystals with Cr-spinel inclusions may be overgrown by hornblende or clinopyroxene and biotite may be rimmed by hornblende or fine-grained pyroxene. Orthopyroxene, clinopyroxene and Fe-Ti-oxides occur in most samples. Plagioclase, hornblende or biotite commonly contain inclusions of apatite, and occasionally also of zircon (Fig. 3d). Cathodoluminescence imaging shows that the zircons exhibit oscillatory zoning (Fig. 3i, j), sometimes superimposed on sector zoning; no core-rim structures were observed in any of the zircons.

Enclaves typically show mineralogical coherence with their host rock in terms of the abundance of hydroxyl-bearing minerals. Their crystal size is variable, and smaller enclaves typically contain crystals with higher aspect ratios but larger crystals, similar to those seen in the host rock, also occur (Fig. 3e). Glass is more common in the enclaves than in the host rocks, and many enclaves have a vesicular texture.

Phase C is the only one to contain appreciable pyroclastic deposits in addition to lava flows. There are minor pumice lapilli beds near Akri Pounda (Fig. 1b), originating from a pyroclastic fall, consisting for 85-95% of juvenile, well-sorted, typically light grey pumice fragments between 1 and 6 cm in size. Lithics are typically oxidised lava blocks, similar to those found in the earlier Phase A and B deposits. The pumice is rich in glass and its crystal cargo is dominated by plagioclase, orthopyroxene and Fe-Ti-oxide; olivine (Fig. 3c), clinopyroxene, quartz and hydroxyl-bearing minerals are rare. However, some intergrowths of plagioclase and orthopyroxene appear to be pseudomorphs, likely after hornblende. Phase C lavas and pyroclastic density current deposits are found near Akri Pounda and Agios Andreas, and consist of coarser and more mafic material than the fallout deposits, which they overlie. Plagioclase and clinopyroxene dominate the mineralogy, with olivine, sometimes as skeletal crystals,

as the third most abundant phase (Fig. 3f). These are the same minerals as those found in the Phase C lava flows, particularly at Palaeo Kastro. Several samples from the density current deposits contain quartz, mantled by clinopyroxene (Fig. 3b). Anhydrous pseudomorphs after larger crystals of hornblende and biotite are scarce.

Within one of the Phase C lavas at Palaeo Kastro, a holocrystalline, phaneritic igneous enclave (sample IM376) was found, contrasting in texture with the common porphyritic enclaves. It consists of a more coarse-grained tonalitic part (plagioclase, quartz, clinopyroxene pseudomorphs of hornblende; Fig. 3g), which is separated by a quartz vein from a finer-grained dioritic part (plagioclase, clinopyroxene, partially pseudomorphosed hornblende). The two parts were analysed separately.

Sampled country rocks comprise Mesozoic limestones and sandstones. Xenoliths are uncommon within the volcanic deposits, and consist mainly of limestones and calcareous sandstones, comparable to the country rocks.

5. Geochemistry

Our approach to sampling was not geared towards a representative selection proportional to the volume of the eruptive products. We tested compositional variability in a single volcanic phase by more dense sampling of Phase D, where we collected 41 samples out of the total of 98 igneous samples. As sampling has been carried out prior to the new volcanic stratigraphy of Pe-Piper and Piper (2013), we failed to sample their Phase E, and Phase F is only represented by a single sample. As we concentrate on the isotopic composition of the magmas, data from previous studies (Dietrich et al., 1988; Francalanci et al., 2005; Pe-Piper, 1975), which do not report complete Sr-Nd-Hf-Pb isotopic data, have not been used. All geochemical data are given in Supplementary Materials S3-6.

223

224 *5.1. Major and trace elements*

225 Our analysed samples vary in silica content between 50 and 68 wt.%. The more
226 mafic samples (<57 wt.% SiO_2) are represented by the enclaves, the Phase C lavas
227 and pyroclastic flow deposits and a few samples from Phase B. Analyses with <54
228 wt.% SiO_2 comprise enclaves only. The densely sampled Phase D deposits span the
229 full range in silica content, from enclave DPM36 at 50.5 to host rock DPM42 at 60.1
230 wt.% SiO_2. MgO concentrations vary between 8 and 1 wt.% (Fig. 4a), with Mg#
231 (molar MgO/(MgO+FeO*)) ranging between 69 and 42. Scatter is pronounced in all
232 variation diagrams, making it hard to argue for curved or inflected differentiation
233 trends. TiO_2 concentrations show a rather monotonous decrease from 0.9 to 0.4
234 wt.% with increasing SiO_2 content (Fig. 4b), whereas K_2O continuously increases
235 from 0.9 to 2.7 wt.% (Fig. 4c), which corresponds to the medium-K trend of Gill
236 (1981). The two parts of the holocrystalline enclave IM376 stand out with respect to
237 their very low potassium content. Apart from a single low-Ca sample in Phase B, all
238 analyses show an aluminium saturation index (molar $Al_2O_3/(Na_2O+K_2O+CaO)$) of
239 less than 1. In terms of FeO*/MgO ratios, Methana defines a typical calc-alkaline
240 (Miyashiro, 1974) or low-Fe (Arculus, 2003) trend, and it classifies as being calcic in
241 the MALI classification of Frost et al. (2001).

242 For Methana as a whole, scatter is even more pronounced for trace elements when
243 compared to major elements, especially for the compatible elements such as Cr and
244 Ni: at an SiO_2 content around 54 wt.%, Cr varies between 400 and 20 ppm (Fig. 4d).
245 However, the basaltic andesites of Phase C are noticeably more homogeneous than
246 enclaves at the same silica content. Using MgO or Mg# on the x-axes gives some
247 reduction of scatter for the compatible (but not for the incompatible) trace elements,
248 but the Phase C products remain more homogeneous. Some of the Phase A

249 samples stand out in having elevated contents of some compatible elements (Cr 80,
250 Ni 50 ppm) at ca. 65 wt.% SiO_2. These samples also have significantly elevated Sr
251 contents (ca. 500 vs 300 ppm; Fig 4e). Other characteristics that stand out are high
252 Rb, Be and especially Cs, U and Pb (Fig. 4f) contents for the youngest (Phase H)
253 volcanics and enclaves, although K_2O (Fig. 4c) and Th are only marginally higher
254 than the main trend. Most trace elements display the expected compatible (Cr, Ni,
255 Sc, Co) or incompatible (Rb, Cs, Be, Ba, Nb, light rare earth elements (LREE))
256 behaviour with increasing SiO_2 contents, but Zr concentrations show an inflection at
257 60 wt.% SiO_2 (Fig. 4g), whereas Y (Fig. 4h) and the middle to heavy rare earth
258 elements generally decrease. Sr (Fig. 4e) and Eu show a scattered, marginally
259 decreasing trend with increasing SiO_2 content. Ratios of MREE/HREE such as Dy/Yb
260 are very scattered (Fig. 4i) but have a tendency to decrease with increasing SiO_2
261 content, apart from the data for Phase C, which show a clear increase in Dy/Yb ratios
262 (as well as Y contents).

263 Rare earth element patterns all show clear LREE over HREE enrichment (Fig. 5),
264 with typically a slightly concave-upward shape for the MREE-HREE patterns (apart
265 from phase C). All samples show a negative Eu anomaly, but this is more
266 pronounced for the more felsic samples. Primitive mantle-normalised trace element
267 diagrams (Fig. 6) show the expected hallmarks of subduction-related magmas, with
268 negative Nb-Ta and Ti anomalies, and a positive one for K and Pb. Nearly all
269 samples also have a negative Ba anomaly. The mafic-intermediate samples show a
270 positive Sr anomaly.

271

272 *5.2. Radiogenic isotope ratios*

In terms of radiogenic isotope ratios, most of the data form a broad concave trend between $^{87}Sr/^{86}Sr$ = 0.7055 at $^{143}Nd/^{144}Nd$ = 0.51266 and $^{87}Sr/^{86}Sr$ = 0.7093 at $^{143}Nd/^{144}Nd$ = 0.51224 (Fig. 7a), but the high-Sr samples from Phase A are displaced towards lower $^{87}Sr/^{86}Sr$ (0.7050) relative to the main array, and the Phase H samples appear to have high $^{143}Nd/^{144}Nd$ for their Sr isotope ratios. The holocrystalline enclave IM376 is virtually indistinguishable from its host rock with regards to Sr and Nd isotopic ratios. Local limestones have $^{87}Sr/^{86}Sr$ of 0.707-0.708 (Fig. 7b), typically with Nd contents too low to determine their Nd isotope signature. More siliciclastic country rocks and xenoliths within some of the volcanic deposits extend the array to slightly more 'crustal' values than the volcanics, with values for $^{87}Sr/^{86}Sr$ = 0.710 at $^{143}Nd/^{144}Nd$ = 0.51221 (Fig. 7a).

Generally the values for $^{87}Sr/^{86}Sr$ (Fig. 7c) and $^{143}Nd/^{144}Nd$ become gradually more 'crustal' with increasing differentiation. The Phase C pumice, however, exhibits abnormally high $^{87}Sr/^{86}Sr$ and low $^{143}Nd/^{144}Nd$ ratios when comparing its SiO_2 and MgO content and its Mg#, to comparable samples from the other units. Even for samples from a single eruptive phase, the correlation between Sr or Nd isotope ratios and fractionation indices is poor. For the whole data set, the negative correlation between Nb content and Nd isotopic composition (Fig. 7d) shows the highest correlation coefficient (r^2 = 0.41) for an element (or elemental ratio) and a radiogenic isotope ratio.

Our slightly more restricted set of Hf isotopic data shows a positive correlation with Nd isotope ratios (Fig. 7e). There is some scatter, but there is no clear distinction between the samples from different phases. Most volcanic samples fall towards the high εHf side of the terrestrial array of Vervoort et al. (2011), especially at the higher end (εNd > -2) of the array. One of the calc-silicate xenoliths found in the Phase C pumice airfall shows the clearest offset from the terrestrial array.

Pb isotope ratios show a poor correlation (Fig. 7f, g). Data for some volcanic phases are better clustered than for others, but these are samples that were derived from a restricted geographical area and the spatial distribution of the samples appears to be the most important parameter with respect to the Pb isotope ratios. Both parts of holocrystalline enclave IM376 (see inset in figs. 7f, g) have ratios of $^{207}Pb/^{204}Pb$ (15.55) and $^{208}Pb/^{204}Pb$ (38.3) that are significantly lower than those of the volcanic samples (>15.67 and >38.7 respectively). The Phase C basaltic andesite sampled in the vicinity of the xenolith, IM379, has the lowest Pb isotope ratios of all the volcanic samples. Three samples from Phase A and B, also taken along the west coast of the peninsula, bridge the isotopic gap between the phase C sample and the rest of the Pb isotopic data array. Trends of Pb isotope ratios against $^{87}Sr/^{86}Sr$ or $^{143}Nd/^{144}Nd$ are scattered (Fig. 9b), but the Phase C pumice with the most crustal Sr and Nd isotope ratios has the highest Pb isotope ratios. There are no obvious correlations when Pb isotope ratios are plotted against differentiation indices, or ratios of trace elements with contrasting aqueous mobility (e.g. Pb/Ce, Sr/Y or Th/U; not shown).

For five samples, 20 to 80 zircons per sample were analysed for their Hf isotope ratios by LA-MC-ICPMS in order to assess their variability (e.g. Rojas-Agramonte et al., 2017) and their similarity to the Hf isotope whole rock analyses (Fig. 7h). The limited amount of material analysed with LA-MC-ICPMS and the correction for interfering ions cause larger uncertainties on the measured ratio for each zircon spot analysis compared to whole rock solution analyses, thereby giving a greater uncertainty for the average Hf isotopic ratio for the zircons compared to the whole rock analyses. However, the standard deviation of the laser ablation $^{176}Hf/^{177}Hf$ analyses for the zircon population from each sample can be compared to that for zircon reference materials such as the Mud Tank or Temora-2 zircon (around 0.008%

during the course of the LA-MC-ICPMS analyses). The data for the five unknowns show a somewhat larger standard deviation, between 0.009 and 0.013%, indicating that the population is relatively homogeneous. Considering the uncertainties, the average Hf isotopic composition for the population of zircons from each of the five samples are very similar.

Taking the uncertainty of the LA-MC-ICPMS measurements into account, the Hf isotope ratios of the zircons are similar to the ratio of the whole rock for the samples with 60-65 wt.% SiO_2, but only in the case of the Phase A sample with 64 wt.% SiO_2 (DPM28) are the values of the zircons as well as the high- and low-pressure dissolution of the whole rock equal within analytical uncertainty. For the other two intermediate samples (IM29 and IM313 from Phase H and Phase D respectively), the zircons have slightly lower Hf isotope values than the HP dissolution, which in turn is lower than the LP dissolution. In the case of the zircons found in a Phase C basaltic-andesite (IM36, with 55 wt.% SiO_2) the zircons' $^{176}Hf/^{177}Hf$ (0.282739 ± 38) is markedly lower than for the host rock; this distinction is more marked for the low-pressure (0.282896) than the high-pressure dissolution (0.282868) of the host rock, indicating that the zircons have a more 'crustal' signature (lower $^{176}Hf/^{177}Hf$) than their host. The systematics are opposite for the phase D sample with 68 wt.% SiO_2 (DPM42), where the zircons have an average higher Hf isotope ratio than the host rocks; also here, the HP dissolution of the host rock is closer to that of the zircons than the LP dissolution.

6. Discussion

6.1. Mixing and assimilation

Field and petrographic evidence (presence of enclaves, ubiquitous mineralogical disequilibrium textures; Fig. 3b,c) shows that magma mingling and magma mixing were important processes in the petrogenesis of the Methana lavas, and this is supported by, for instance, the lack of inflection points on the Harker diagrams of TiO_2 and Y (Fig. 4b,h). Magma mixing was likely accompanied by the selective entrainment of certain minerals to explain excess scatter in the Harker variation diagrams, as has also been mentioned by previous workers (Pe-Piper and Piper, 2013). Besides, the different phases may also have had different primary magmas, as exemplified by the elevated Pb concentrations of the Phase H deposits. Ignoring the complications of different primary magmas, fractionation and selective entrainment of minerals for the moment, we will first assess the broad trends seen in the radiogenic isotope data in order to identify end members and constrain the processes that yielded these trends, refining the models proposed by Elburg et al. (2014). Parameters for the simple mixing and Assimiliation-Fractional Crystallisation (AFC; DePaolo, 1981) models can be found in Table 1. For the AFC models, bulk distribution coefficients were taken as 0.3 for Nd, 0.001 for Th and 1.7 for Sr except for the high pressure (HP) AFC model, where it was 0.1. These values are based on the general trends seen in the variation diagrams, and are in broad agreement with the observed mineral assemblages (olivine, clinopyroxene, orthopyroxene, plagioclase, hornblende).

6.1.1. Exploring evolved end members

The majority of the Sr and Nd isotopic data can be explained by simple mixing between the two isotopically extreme samples from the Phase C deposits (Fig. 7a), namely the basaltic andesites with relatively low Sr isotope ratios (0.7057) and high Nd isotope ratios (0.51260), and the most isotopically evolved pumice ($^{87}Sr/^{86}Sr$ =

375 0.7093, $^{143}Nd/^{144}Nd$ = 0.51224). This yields a mixing line on which the majority of the
376 samples fall. The isotopically most primitive samples are similar to those analysed by
377 Woelki et al. (2018), and the reader is referred to this publication for an in-depth
378 discussion on the primary magma to the Methana volcanics.

379 Evidence for mixing of a geochemically and isotopically more evolved magma with
380 the basaltic andesites comes from petrographic data (Fig. 3b, c), as well as from the
381 observation that zircons with a much lower Hf isotope ratio than the whole rock were
382 found within mafic sample IM36 (Fig. 7h). The relative isotopic homogeneity of this
383 zircon population, combined with the petrographic observations of the elongated
384 euhedral shape of the zircons (Fig. 3d), the CL-imaging that shows magmatic
385 oscillatory zoning without any core-rim structure (Fig. 3i, j), and the maximum age of
386 5 Ma, shows that these zircons are unlikely to be xenocrysts derived from the country
387 rocks. Although a simple mixing line satisfactorily models most of the Methana
388 samples within Sr-Nd (and also Hf) isotopic space, scatter in diagrams of Sr-Nd-Hf
389 isotope ratios against an index of fractionation indicates that this cannot be the whole
390 story. For instance, the isotopically most evolved pumice samples of Phase C are not
391 the most evolved in terms of SiO_2 (Fig. 7c) or incompatible trace elements. We will
392 use Th as an index of fractionation (Fig. 8a), as Pe-Piper and Piper (2013) noticed a
393 correlation between the concentration of Th and the volume percentage of enclaves
394 in the deposits, and suggested that Th could trace the role of AFC (Assimilation +
395 Fractional Crystallisation) processes. In this model, the repeated input of less
396 fractionated magma (now represented by the enclaves) would provide the thermal
397 energy necessary for assimilation.

398 The first thing the $^{143}Nd/^{144}Nd$ versus Th diagram (Fig. 8a) shows is that the
399 interpretation of the Phase C products representing simple mixing between two end
400 members is not quite accurate, as the isotopically most primitive basaltic andesites

401 from Agios Andreas in the north (to which zircon-bearing sample IM36 belongs) have
402 a higher Th content than the basaltic andesites from Akri Pounda in the south , which
403 have slightly lower $^{143}Nd/^{144}Nd$. The latter seem to form a mixing line (curve i in Fig.
404 8a) with the Akri Pounda pumice samples, whereas the former lie on a mixing trend
405 (curve ii in Fig. 8a) with the Palaeo Kastro andesites at higher Th contents. The high-
406 Th end of the trend can be extended to the field for the Miocene granitoids, but these
407 are unlikely to be the material directly involved in the physical mixing process: The
408 zircons from those intrusives have present-day $^{176}Hf/^{177}Hf$ values dominantly between
409 0.2822 and 0.2826 (Bolhar et al., 2012), and are thus significantly less radiogenic
410 than the values for zircons from the Methana samples (0.28265-0.28285).

411

412 Phase D sample DPM42 has among the highest Th contents at intermediate
413 $^{143}Nd/^{144}Nd$; although Phase H sample IM29 has equally high Th contents, it isn't as
414 evolved in terms of SiO_2 content (62 vs 68 wt.%), and also has a higher $^{143}Nd/^{144}Nd$
415 ratio. Sample IM29 falls close to the isotopically less evolved Aegean Miocene
416 granitoids (from Samos and Kos; Altherr and Siebel, 2002) in this diagram, but it is
417 very different in its Sr content (330 vs 450-2000 ppm, not shown). Although a simple-
418 mixing curve between the most mafic (DPM36) and most felsic (DPM42) Phase D
419 samples could explain some of the observed variability in Methana, it does not
420 explain how DPM42 obtained its isotopic characteristics in the first place. Sample
421 DPM42 is also characterised by zircons that are isotopically more primitive (high
422 $^{176}Hf/^{177}Hf$ ratio) than the whole rock composition. This implies that crustal
423 contamination occurred after the onset of zircon crystallisation, which could argue for
424 the operation of AFC-type processes to explain the isotopic characteristics of the
425 evolved end members.

426

We modelled this AFC process by taking calc-silicate country rock IM26 (Upper Jurassic calcareous sandstone) as the crustal end member and Phase D enclave DPM36 as the more primitive melt. This yields a satisfactory fit (curve i in Fig. 8b) for sample DPM42, but only with a high parameter R (rate of assimilation : fractionation) of 0.8, and a remaining melt fraction of slightly less than 60 wt.%, meaning that more than 30% of host rock would need to be assimilated. This high amount of assimilation is mainly a reflection of the very low Th and Nd contents of this crustal end member. If a pelitic, rather than calc-silicate, xenolith (IM362) is taken, the obtained AFC curve is similar, but the amount of assimilated material is reduced to 13%. The curve can be shifted upward (curve ii in Fig. 8b) to pass through sample IM29 by adjusting the R parameter downward to ca. 0.4 (for IM26 as an assimilant) or 0.25 (for IM362). With this lower rate of assimilation, the amount of melt remaining would be smaller; this is contrary to what is observed for the SiO_2 content of Phase H sample IM29 (62 wt.%) versus Phase D sample DPM42 (68 wt.%). It is therefore more likely that Phase H belongs to a different magmatic series, with inherently higher Th contents, rather than being related to the Phase D deposits by a different rate of assimilation to crystallisation (see further discussion in section 6.1.4).

Returning to the very ‘crustal’ Sr-Nd-Hf isotopic characteristics of the Phase C pumices, it would be possible to explain these by a large degree of remelting of some Miocene granitoid and mixing with small amounts of the basaltic andesitic melt. However, this interpretation is not supported by the very moderate contents in the rhyodacites of elements such as K, Rb and Ba (Fig. 8c), which are significantly enriched in all the Miocene granitoids. As these are incompatible elements, AFC-type processes would provide an even worse fit to the data than simple mixing.

The very crustal Sr-Nd-Hf isotopic characteristics of the Phase C pumice end member are best explained by assimilation with material similar to that of the Ios basement, with a $^{143}Nd/^{144}Nd$ ratio of 0.5119 (Klaver et al., 2016). Depending on whether the primitive end member is assumed to be enclave DPM36 (curve iii in Fig. 8b), or a hypothetical composition with a higher $^{143}Nd/^{144}Nd$ of 0.5127 (curve iv), the pumice can be modelled by an R value of 0.8 or 0.4 respectively, and a total amount of assimilation of 5 and 13%. This also fits the Sr isotope data (not shown) if the assimilant has a $^{87}Sr/^{86}Sr$ ratio around 0.74 and a Sr concentration of 100 ppm, which has indeed been measured for the Ios basement (Buettner et al., 2005; Klaver et al., 2016).

In conclusion, the isotopic and trace element data can be explained by the assimilation of material similar to entrained xenoliths for the evolved but isotopically less extreme end members of Phase D and H. However, this explanation does not hold for the very 'crustal' isotopic signature of the Phase C pumice sample, for which an isotopically more extreme contaminant similar to the Ios basement is needed. The observed isotopic arrays are mainly a result of physical mixing between isotopically primitive mafic magmas and the more evolved magmas that obtained their chemical and isotopic characteristics as a result of AFC processes. However, when elemental data are taken into account (e.g. Fig. 8a), it is obvious that variable primary magmas may be involved as well, which will be explored further below in section 6.1.4.

6.1.2. Pb isotopic constraints: Ios basement and localised fluid

Arguments for the involvement of an assimilant similar to the Ios basement rocks can also be made on the basis of the Pb isotopic signature. The majority of samples from

Ios are characterised by having high $^{208}Pb/^{204}Pb$ ratios relative to their $^{206}Pb/^{204}Pb$, reflecting high time-integrated Th/U ratios (Klaver et al., 2016). The $^{208}Pb/^{204}Pb$ ratios of the Methana samples (Fig. 7f, 9a) are higher than those of Santorini and Nisyros, but lower than the field for Crommyonia (Soens, 2015). The Phase C pumice is again an end member in the data set, with the highest $^{206,7,8}Pb/^{204}Pb$ ratios. However, one of the Phase C samples, an andesite from Palaeo Kastro, which is the host to the dioritic-tonalitic crystalline enclave, is significantly offset in Pb isotopic space towards the low Pb isotopic ratios of this enclave. A slightly less pronounced offset is also seen for two Phase A and one Phase B samples. The most obvious factor that these samples have in common is that they were taken near the west coast of the peninsula. However, there are also samples from the same area that do not display this offset. In Pb-Nd isotopic space (Fig. 9b), these aberrant samples give the impression that only the Pb isotopic signature was lowered to offset them from the main array. The crystalline enclave itself would make a very inefficient contaminant, as its Pb content (ca. 3 ppm) is lower than for any of the juvenile samples (> 5 ppm). It appears more likely that some of the juvenile samples were affected by the same, perhaps fluid-related, contaminant that affected the Pb isotopic composition of the crystalline enclave. The isotopic signature of this Pb contaminant suggest a source with only moderate time-integrated U+Th/Pb ratios, not dissimilar to Mid-Ocean Ridge Basalt. The location of this source is as yet unclear, but it could potentially be related to a mafic rock type such as the sliver of ophiolitic mélange exposed on the NW side of the peninsula (Dietrich and Gaitanakis, 1995). The mode of contamination could be by assimilation of fluid-altered volcanic cumulates, which would be difficult to detect in other geochemical parameters.

6.1.3. High-Sr Phase A samples

Some of the phase A host rocks, derived from two flows near the village of Loutses, have notably lower Sr isotopic ratios and higher Sr concentrations than the other rocks, and fall outside of the main data trend in many diagrams (Fig. 7a, b). This group of samples is also unusual in having high MgO, Cr and Ni contents (Fig. 4a, d) for their SiO_2 contents of 65 wt.%, which is likely related to the presence of olivine and clinopyroxene, overgrown by hornblende, observed in the samples.

One of the samples from this group (DPM28) was analysed for its Hf isotopic characteristics by LP and HP whole rock dissolution as well as for the individual zircon crystals, and gave no detectable differences between these analyses. Therefore, the higher compatible element contents could reflect entrainment of clinopyroxene and olivine cumulates, as these minerals would contribute negligibly to the Hf budget. Further characteristics of these samples are moderately low Y contents, similar to Phase D samples of the same silica content, but significantly higher Dy/Yb ratios than most Phase D samples. Low Dy/Yb ratios are typical for melts that underwent amphibole fractionation (Davidson et al., 2007), which has been argued to have been an important process for the Methana lavas (Elburg et al., 2014), whereas a low Y content in combination with high Dy/Yb ratios points towards a role for garnet fractionation. Therefore, the high-Sr samples may document a phase of fractionation at higher pressure during which plagioclase was not stable, and hence Sr would have been an incompatible element. This can be modelled with a primitive magma with Sr and Nd isotopic compositions as primitive as 0.7035 and 0.5129 respectively, and only 300 ppm Sr in this mafic magma, which increases to the observed ca. 500 ppm during the high pressure phase of AFC, using an Ios-style assimilant (Fig. 8d, Table 1). The slight increase of the $^{87}Sr/^{86}Sr$ ratio with decreasing Sr concentrations within this group is likely related to a subsequent phase of fractionation where plagioclase was crystallising. Alternatively, these samples could

have been derived from a different primary magma with higher Sr concentrations, making crustal contamination less visible in the Sr isotope signature.

6.1.4. Phase H

Both the host rock and the enclaves of Phase G and Phase H are similar in their silica and MgO content, and the differences in their trace element concentrations can thus be illustrated by a normalised trace element diagram (Fig. 10) without the need to correct for differences in degree of fractionation. Here the average of the Phase H host rocks is normalised over the average of the Phase G host rocks, and the same for the enclaves. This shows that the Phase H enclaves and host rocks both show clear enrichments in certain elements compared to their Phase G equivalents, with Cs >U >Pb = Be > Rb > Th >Sr > Ba = K. For the other elements, apparent enrichments and depletions fall within the standard deviation of the corresponding averages. Since the most incompatible elements are not those that are the most enriched, smaller degrees of partial melting of an invariant source cannot be the main cause for the distinctions between Phase G and H. Some of the enriched elements are considered to be 'fluid mobile' (Cs, U, Pb), but other elements that show equal enrichments, such as Be and to a lesser extent Th, are considered fluid immobile (Ryan and Chauvel, 2014), whereas still other fluid-mobile elements such as Li do not show significant enrichment. The lack of enrichment in the latter element could be related to amphibole fractionation. However, the other discrepancies are more difficult to explain if we would want to invoke a fluid component, for instance derived from the subducted slab. The observed enrichments are broadly similar to those seen in the (significantly more felsic) Crommyonia volcanics (Soens, 2015), which appear to show the most pronounced imprint of assimilation of Ios-like material based on their low Nd isotope ratios (Fig. 9b). Clearly, the Phase H volcanics have

555 significantly higher Nd isotopic ratios than the Crommyonia volcanics, but they do
556 trend towards the Crommyonia field in terms of Pb isotopic composition (Fig. 9a).
557 Remarkably, the Phase H *enclaves* are actually more similar to the Crommyonia
558 volcanics than the *host rocks* in terms of Pb isotopic composition. This could
559 potentially be related to two consecutive phases of assimilation, first with an Ios-like
560 contaminant followed by a contaminant more similar to xenolith IM362 for the host
561 rocks. However, we have not been able to find assimilants of which the whole rock
562 composition matches the pattern seen in Fig. 10 in our own data set, nor in the Ios
563 basement samples analysed by Klaver (2016) or among the Miocene granitoids
564 published by Altherr and Siebel (2002). Perhaps selective assimilation of a partial
565 melt of any of these rock types, with a specific residual phase such as rutile or
566 allanite, could explain the patterns. However, our lack of knowledge of either the
567 likely assimilant(s) or the processes involved does not permit more detailed
568 modelling.

569

570 *6.2. Geochemistry versus time and the relationship with tectonics*

571 The data presented here do not show any clear unidirectional progression with time
572 in the geochemistry of the magmas (Fig. 11), with the oldest and youngest deposits
573 (Phase A vs H) having similar and, for Methana, relatively high Nd isotope ratios
574 (epsilon Nd 0 to -2). Although the youngest volcanic phase (Phase H) appears quite
575 distinct in terms of its geochemical signature, as discussed above, it does not
576 represent the culmination of a progressive enrichment trend through time, as
577 samples from Phase G and phase D cannot be distinguished from each other in
578 terms of their incompatible trace element signature.

579 The changes in tectonic regime, documented by Pe-Piper and Piper (2013), mainly
580 appear to affect the Phase C deposits, interpreted to have erupted during the onset
581 of strike-slip faulting. These deposits also stand out from the others from a
582 volcanological point of view, with their higher content of explosive products (air fall
583 pumice and pyroclastic flow deposits). The air fall pumice deposits were erupted at
584 the start of Phase C, and contain samples with the most crustal Sr and Nd isotopic
585 signatures, even though they are not the most felsic ones (60-63 wt.% SiO_2). The
586 basaltic-andesitic lava flows and pyroclastic flow deposits are among the most mafic
587 (ca. 55 wt.% SiO_2) and isotopically most primitive on the island. They represent the
588 only eruptive phase during which mafic magmas formed their own deposits; other
589 mafic rocks are only found as enclaves within more evolved flows. This fits in with the
590 idea that the faulting taking place during phase C facilitated magma ascent and
591 eruption of these mafic magmas. During periods of compression, magmas stalled at
592 intermediate depths and suffered 'rheological death' as a result of hornblende
593 crystallisation. They could only erupt after being remobilised by a pulse of more mafic
594 magma, which we now find as enclaves within the intermediate-felsic deposits
595 (Elburg et al., 2014; Fig. 12).

596 The eruption of the isotopically most evolved magmas during this period of extension
597 is somewhat surprising, as it seems more logical that lavas would experience higher
598 degrees of crustal contamination as a result to hindered ascent during periods of
599 compression. The presence of olivine in some of the pumice samples, combined with
600 the fact that their pyroclastic fall deposits are directly overlain by pyroclastic density
601 current deposits containing juvenile basaltic-andesite clasts, of which some contain
602 quartz, suggests that the two contrasting magmas formed part of a single eruptive
603 phase. Contrasting with the case of mafic enclaves within a more felsic host rock, this
604 semi-simultaneous eruption of contrasting magmas could have been initiated by
605 felsic magma entering a magma chamber filled with mafic magma (Eichelberger et

606 al., 2000; Fig. 12). The pumice samples are also somewhat different from other
607 samples at similar SiO_2 contents and fall on the low-Sr, high-Y and high-Dy/Yb side
608 of the data set. Although higher Y contents can be associated with a dry fractionation
609 series (with pyroxene rather than amphibole as the main ferromagnesian phase), the
610 offset from the main array is too small to invoke a significant role for this process: a
611 typical hornblende-poor fractionation series such as seen on the island of Santorini
612 contains twice as much Y at 60-65 wt.% SiO_2 (Elburg et al., 2014) as the rather
613 modest 25 ppm seen in the Phase C pumice. The presence of pseudomorphs of
614 plagioclase and pyroxene, presumably after hornblende, supports the idea of
615 amphibole fractionation, but the higher Dy/Yb ratios of these deposits could possibly
616 indicate a minor role for garnet fractionation. Taken together, the trace element and
617 isotopic data may be explained by a prolonged period of AFC-type processes in a
618 magma chamber located at a deeper crustal level, with host rocks more similar to the
619 Ios basement than to the exposed Mesozoic country rocks and the entrained
620 xenoliths.

621 This idea of prolonged storage is supported by the age gap between the Phase A
622 (ca. 3.5 Ma) and Phase C deposits (ca. 1.4 Ma) (Pe-Piper and Piper, 2013): The
623 Phase C pumice deposits represent the first evidence of renewed magmatic activity,
624 and could represent magmas that were arrested in the deeper crust during the
625 waning stages of Phase A. During solidification, they had ample opportunity to ingest
626 the country rocks. The renewed magmatic activity during Phase C brought mafic
627 magma in contact with these solidified intrusions, which were remelted, and followed
628 the same pathway to the surface as the more mafic magmas, eventually erupting
629 coevally. Hence, it seems that during times of extension, we clearly see the effects of
630 mafic-felsic interaction at a deep crustal level, giving rise to explosive activity,
631 whereas during a compressional regime, effusive igneous activity only documents
632 the processes that are taking place at a shallow level in the crust (Fig. 12). Although

633 deeper assimilation also happens during compressional stages, the results thereof
634 never make it to the Earth's surface, but may be forming granitoids that only become
635 exposed after uplift and erosion.

636

637

638 **7. Conclusions**

639 The volcanic deposits of Methana peninsula show a wide variation in their
640 geochemical and isotopic characteristics and contain the most 'crustal' rock types of
641 the active South Aegean Volcanic Arc in terms of Sr-Nd-Hf composition, trending
642 towards the values for the extinct, more evolved centres of Crommyonia. In
643 combination with the high $^{207,8}Pb/^{204}Pb$ versus $^{206}Pb/^{204}Pb$ isotopic compositions, the
644 data point towards an important role for assimilation of crustal rocks similar to those
645 of the Cycladic Basement of Ios, although these are nowhere exposed on Methana.
646 Assimilation of Mesozoic rocks, as exposed on Methana and entrained as xenoliths,
647 is likely to also have played a role. Assimilation thus took place at different crustal
648 levels, and some of the deeper stages of evolution may also have influenced the
649 crystallising mineral assemblages, with plagioclase-free fractionation resulting in high
650 Sr concentrations in some of the older samples. There is no temporal geochemical
651 trend in the volcanic deposits, although the youngest samples show unusual
652 enrichments of some elements, of which the source cannot be determined with
653 certainty.

654 The period of extension, during which the Phase C deposits erupted (Pe-Piper and
655 Piper, 2013), had an important effect on the igneous products, which were explosive,
656 rather than effusive, and contain isotopically more primitive mafic rocks as well as
657 pumice with the most 'crustal' isotopic signature. The latter likely obtained their

signature by stalling of the magma at deeper crustal levels during an earlier tectonic compressional phase, where they assimilated Ios-type crust. They were remobilised by mafic magmas during the extensional period, and followed the same path towards higher crustal levels. Their emplacement took place explosively, forming deposits that are more similar to those seen on the island of Santorini, of which the crust is in a permanent state of extension (Feuillet, 2013), than to the typical lava domes of Methana. However, the chemical and isotopic composition of the Methana pumice deposits is very different from those of Santorini, as the Santorini magmas evolved by predominantly shallow-level fractionation of pyroxene, rather than amphibole, leading to Y enrichment in the more differentiated products. Moreover, even the most evolved Santorini lavas typically have less crustal Sr-Nd-Hf isotopic compositions than the most primitive Methana products. Both characteristics are likely related to the thickness of the crust which is much thinner under Santorini (20 km) than under Methana (30 km) (Karagianni et al., 2005).

The case of Methana clearly shows how the geochemical and isotopic characteristics of a subduction-related volcano may vary in accordance with regional changes in tectonic regime. The ability to recognise these characteristics and their relationship to the tectonic conditions in a modern arc will enable us to use geochemical data of igneous rocks from the earlier geological record to make inferences about their palaeotectonic setting.

Acknowledgments:

This research formed part of Smet's PhD work, who was funded by a BOF bursary; research costs were borne by FWO grants G.0585.06N, G.0669.06 and 1509007N.

683 Hf isotopic analyses were performed at the Vrije Universiteit Amsterdam funded by
684 TransNational Access project 079-TNA3 of EuroPlanet. Laboratory work was
685 assisted by Mr Kris Latruwe (Ghent), Mr Richard Smeets (Amsterdam) and Ms Siri
686 Simonsen (Oslo). Thin sections were prepared by Mr Jan Jurceka. Olga Zlatkin and
687 Robert Bolhar are thanked for their constructive reviews.

688

689

690 **Table captions:**

691

692 Table 1: Mixing end members for curves in Figures 7 and 8.

693

694

695 **Figure captions:**

696

697 Fig. 1a: Overview map of the Aegean area; b: Geological map of Methana after Pe-
698 Piper and Piper (2013) and Dietrich and Gaitanakis (1995) with samples indicated.
699 Sample pre-fix abbreviations: d=DPM; i=IM.

700

701 Fig. 2: Variable textures and sizes of enclaves in lavas from Phase D (a) and Phase
702 H (b).

703

704 Fig. 3: Thin section (a-g) and cathodoluminescence (h-i) images. PPL = plane
705 polarised light; XPL = crossed polars. a: host rock sample DPM28 from Unit A with
706 plagioclase and hornblende, which is almost completely replaced by opacite (PPL);
707 b: scoriaceous sample IM359 from the mafic deposits of Unit C, showing a rounded
708 quartz crystal rimmed by fine-grained pyroxenes (XPL); c: dacitic pumice sample
709 IM17b from Unit C, with a xenocryst of olivine, mantled by clinopyroxene and
710 hornblende (PPL); d: host rock sample IM29 from Phase H with euhedral zircon

711 enclosed in a large crystal of hornblende (PPL); e: enclave sample DPM35 from
712 Phase D, with a large hornblende crystal, now partially altered to opacite in a matrix
713 of smaller plagioclase and hornblende (PPL); f: sample IM36 from the mafic Agios
714 Andreas lavas of Phase C, showing the typical mineralogy of olivine, clinopyoxene
715 and plagioclase (XPL); g: holocrystalline enclave IM376 with plagioclase, quartz and
716 clinopyroxene (XPL); i and j: typical zircon crystals in samples IM29 (Phase H) and
717 IM313 (Phase D) respectively.

718

719 Fig. 4: Harker variation diagrams for igneous samples. Major element oxides in
720 weight percent and trace elements in ppm. Fields in K_2O diagram after Gill (1981).
721 Individual samples of which the isotopic characteristics are referred to in the text
722 have been indicated with their sample names.

723

724 Fig. 5: Normalised rare earth element diagrams for the different volcanic host rocks
725 and their enclaves. Normalising factors from Evensen et al. (1978).

726

727 Fig. 6: Normalised trace element diagrams. Normalising factors from Palme and
728 O'Neill (2014).

729

730 Figure 7: Bivariate diagrams relating to radiogenic isotope ratios. Fields shown are
731 for Santorini (S) and Nisyros (N) from the authors' data compilation. a: $^{143}Nd/^{144}Nd$
732 versus $^{87}Sr/^{86}Sr$ (note that limestones cannot be shown because Nd contents are too
733 low to determine their isotopic composition) with curve showing simple mixing for the

Phase C deposits (see Table 1 for end members); b: $^{87}Sr/^{86}Sr$ versus Sr concentration; c: $^{87}Sr/^{86}Sr$ versus SiO_2; d: $^{143}Nd/^{144}Nd$ versus Nb; e: whole rock epsilon Hf versus epsilon Nd, with the terrestrial array after Vervoort et al. (2011); f: $^{207}Pb/^{204}Pb$ versus $^{206}Pb/^{204}Pb$, with inset to show the outlying holocrystalline enclave; g: $^{208}Pb/^{204}Pb$ versus $^{206}Pb/^{204}Pb$, with inset to show the outlying holocrystalline enclave; h: average LA-MC-ICPMS $^{176}Hf/^{177}Hf$ ratio of zircon versus whole rock values, for both high-pressure (HP; dark colours) and low pressure (LP; light colours) dissolutions. The grey field around the equal-Hf-isotope line shows the uncertainty of the laser-ablation analyses. The 'add zircon' arrows indicate the way in which the whole rock Hf isotopic signature changes by adding zircon.

Fig. 8: a: $^{143}Nd/^{144}Nd$ versus Th concentrations with curves showing simple mixing models (see Table 1 for end members); b: as a, but with AFC models; c: $^{143}Nd/^{144}Nd$ versus K_2O concentration to show unsuitability of Miocene granitoids as mixing end members; d: $^{87}Sr/^{86}Sr$ versus Sr concentration illustrating high pressure AFC model for the high-Sr Phase A samples.

Figure 9: Isotope diagrams showing potential contamination by Ios basement and an unknown unradiogenic Pb end member. a: $^{208}Pb/^{204}Pb$ versus $^{206}Pb/^{204}Pb$; b: $^{143}Nd/^{144}Nd$ versus $^{208}Pb/^{204}Pb$.

Fig. 10: Trace element diagram, normalised over Phase G deposits, to show the enrichments of Phase H, resembling those of Crommyonia samples from Soens (2015).

758

759 Fig. 11: Epsilon Nd and Ce/Pb ratios of the various igneous units, arranged in
760 temporal order. No unidirectional temporal trend can be seen.

761

762 Fig.12: Cartoon illustrating the envisaged magmatic development during
763 compressional (left) and extensional (right) phases, after Eichelberger et al. (2000).
764

765

766 **References:**

767

768 Altherr, R., Siebel, W., 2002. I-type plutonism in a continental back-arc setting: Miocene
769 granitoids and monzonites from the central Aegean Sea, Greece. Contributions to
770 Mineralogy and Petrology 143, 397-415.

771 Arculus, R.J., 2003. Use and Abuse of the Terms Calcalkaline and Calcalkalic. Journal of
772 Petrology 44, 929-935.

773 Bolhar, R., Ring, U., Allen, C.M., 2010. An integrated zircon geochronological and
774 geochemical investigation into the Miocene plutonic evolution of the Cyclades, Aegean
775 Sea, Greece: Part 1: Geochronology. Contributions to Mineralogy and Petrology, DOI
776 10.1007/200410-200010-200504-200414.

777 Bolhar, R., Ring, U., Kemp, A.I.S., Whitehouse, M.J., Weaver, S.D., Woodhead, J.D., Uysal,
778 I.T., Turnbull, R., 2012. An integrated zircon geochronological and geochemical
779 investigation into the Miocene plutonic evolution of the Cyclades, Aegean Sea, Greece:
780 part 2—geochemistry. Contributions to Mineralogy and Petrology 164, 915-933.

781 Buettner, A., Kleinhanns, I.C., Rufer, D., Hunziker, J.C., Villa, I.M., 2005. Magma generation
782 at the easternmost section of the Hellenic arc: Hf, Nd, Pb and Sr isotope geochemistry of
783 Nisyros and Yali volcanoes (Greece). Lithos 83, 29-46.

784 Davidson, J., Turner, S., Handley, H., Macpherson, C., Dosseto, A., 2007. Amphibole
785 "sponge" in arc crust? Geology 35, 787-790.

786 Defant, M.J., 1992. The geochemistry of young volcanism throughout western Panama and
787 southeastern Costa Rica: an overview. Journal - Geological Society (London) 149, 569-
788 579.

789 DePaolo, D., 1981. Trace element and isotopic effects of combined wallrock assimilation and
790 fractional crystallisation. Earth and Planetary Science Letters 53, 189-202.

791 Dietrich, V., Gaitanakis, P., 1995. Geological Map of Methana Peninsula (Greece). ETH,
792 Zürich, Switzerland.

793 Dietrich, V.J., Mercolli, I., Oberhänsli, R., 1988. Dazite, High-Alumina-Basalte und Andesite
794 als Produkte amphiboldominierter Differentiation (Aegina und Methana, Ägäischer
795 Inselbogen). Schweizerische Mineralogische und Petrographische Mitteilungen 68, 21-39.

796 Eichelberger, J.C., Chertkoff, D.G., Dreher, S.T., Nye, C.J., 2000. Magmas in collision:
797 Rethinking chemical zonation in silicic magmas. Geology 28, 603-606.

798 Elburg, M.A., Andersen, T., Bons, P.D., Simonsen, S.L., Weisheit, A., 2013. New constraints
799 on Phanerozoic magmatic and hydrothermal events in the Mt Painter Province, South
800 Australia. Gondwana Research 24, 700-712.

801 Elburg, M.A., Smet, I., De Pelsmaeker, E., 2014. Influence of source materials and
802 fractionating assemblage on magmatism along the Aegean Arc, and implications for
803 crustal growth, in: Zellmer, G., Straub, S., Gómez-Tuena, A. (Eds.), Orogenic Andesites
804 and Crustal Growth. Geological Society, London.

805 Elburg, M.A., van Bergen, M.J., Foden, J.D., 2004. Subducted upper and lower continental
806 crust contributes to magmatism in the collision sector of the Sunda-Banda arc, Indonesia.
807 Geology 32, 41-44.

808 Evensen, N.M., Hamilton, P.J., O'Nions, R.K., 1978. Rare-earth abundances in chondritic
809 meteorites. Geochimica et Cosmochimica Acta 42, 1199-1212.

810 Feuillet, N., 2013. The 2011-2012 unrest at Santorini rift: Stress interaction between active
811 faulting and volcanism. Geophysical Research Letters 40, 3532-3537.

812 Francalanci, L., Vougioukalakis, G.E., Perini, G., Manetti, P., 2005. A West-East Traverse
813 along the magmatism of the south Aegean volcanic arc in the light of volcanological,

chemical and isotope data, in: Fytikas, M., Vougioukalakis, G.E. (Eds.), South Aegean Active Volcanic Arc: Present Knowledge and Future Perspectives, pp. 65-111.

Frost, B.R., Barnes, C.G., Collins, W.J., Arculus, R.J., Ellis, D.J., Frost, C.D., 2001. A geochemical classification for granitic rocks. Journal of Petrology 42, 2033-2048.

Gill, J.B., 1981. Orogenic andesites and plate tectonics. Springer-Verlag.

Jolivet, L., Menant, A., Sternai, P., Rabillard, A., Arbaret, L., Augier, R., Laurent, V., Beaudoin, A., Grasemann, B., Huet, B., Labrousse, L., Le Pourhiet, L., 2015. The geological signature of a slab tear below the Aegean. Tectonophysics 659, 166-182.

Karagianni, E.E., Papazachos, C.B., Panagiotopoulos, D.G., Suhadolc, P., Vuan, A., Panza, G.F., 2005. Shear velocity structure in the Aegean area obtained by inversion of Rayleigh waves. Geophysical Journal International 160, 127-143.

Keay, S., Lister, G., 2002. African provenance for the metasediments and metaigneous rocks of the Cyclades, Aegean Sea, Greece. Geology 30, 235-238.

Klaver, M., 2016. Dynamics of magma generation and differentiation in the central-eastern Aegean arc, Faculty of Earth and Life Sciences. Free University Amsterdam, Amsterdam, p. 213.

Klaver, M., Carey, S., Nomikou, P., Smet, I., Godelitsas, A., Vroon, P.Z., 2016. A distinct source and differentiation history for Kolumbo submarine volcano, Santorini volcanic field, Aegean arc. Geochemistry, Geophysics, Geosystems 17, doi:10.1002/ 2016GC006398.

Miyashiro, A., 1974. Volcanic rock series in island arcs and active continental margins. American Journal of Science 274, 321-355.

Mizera, M., Behrmann, J.H., 2015. Strain and flow in the metamorphic core complex of Ios Island (Cyclades, Greece). International Journal of Earth Sciences 105, 2097-2110.

837 Palme, H., O'Neill, H.S.C., 2014. Cosmochemical estimates of mantle composition, in:
838 Carlson, R.W. (Ed.), Treatise on Geochemistry, vol.3, The Mantle and Core. Elsevier, New
839 York, pp. 1-39.

840 Pe-Piper, G., 1975. Strontium isotope ratios in volcanic rocks from the northwestern part of
841 the Hellenic Arc. Chemical Geology 15, 53-60.

842 Pe-Piper, G., Piper, D.J.W., 2002. The igneous rocks of Greece: The anatomy of an orogen.
843 Gebrüder Borntraeger, Berlin, pp. 573.

844 Pe-Piper, G., Piper, D.J.W., 2013. The effect of changing regional tectonics on an arc
845 volcano: Methana, Greece. Journal of Volcanology and Geothermal Research 260, 146-
846 163.

847 Rojas-Agramonte, Y., Williams, I., Arculus, R., Kröner, A., García-Casco, A., Lázaro, C.,
848 Buhre, S., Wong, J., Geng, H., Echeverría, C.M., Jeffries, T., Xie, H., Mertz-Kraus, R.,
849 2017. Ancient xenocrystic zircon in young volcanic rocks of the southern Lesser Antilles
850 island arc. Lithos.

851 Ryan, J.G., Chauvel, C., 2014. The Subduction-Zone Filter and the Impact of Recycled
852 Materials on the Evolution of the Mantle. 479-508.

853 Shinjo, R., 1999. Geochemistry of high Mg andesites and the tectonic evolution of the
854 Okinawa Trough-Ryukyu arc system. Chemical Geology 157, 69-88.

855 Skarpelis, N., Kyriakopoulos, K., 1992. Occurrence and 40Ar/39Ar dating of a granite in Thera
856 (Santorini, Greece). Geologische Rundschau 81, 729-735.

857 Soens, B., 2015. Petrology and geochemistry of the Crommyonia volcanic rocks north of the
858 Saronic Gulf, Greece, Department of Geology. Ghent University, Ghent, Belgium, p. 201.

859 Straub, S.M., Zellmer, G.F., 2012. Volcanic arcs as archives of plate tectonic change.
860 Gondwana Research 21, 495-516.

861 Van Hinsbergen, D.J.J., Hafkenscheid, E., Spakman, W., Meulenkamp, J.E., Wortel, R.,
862 2005. Nappe stacking resulting from subduction of oceanic and continental lithosphere
863 below Greece. Geology 33, 325-328.

864 Vervoort, J.D., Plank, T., Prytulak, J., 2011. The Hf–Nd isotopic composition of marine
865 sediments. Geochimica et Cosmochimica Acta 75, 5903-5926.

866 Woelki, D., Haase, K.M., Schoenhofen, M.V., Beier, C., Regelous, M., Krumm, S.H., Günther,
867 T., 2018. Evidence for melting of subducting carbonate-rich sediments in the western
868 Aegean Arc. Chemical Geology 483, 463-473.

869 Zellmer, G.F., 2009. Petrogenesis of Sr-rich adakitic rocks at volcanic arcs: insights from
870 global variations of eruptive style with plate convergence rates and surface heat flux.
871 Journal of the Geological Society 166, 725-734.

872 Zlatkin, O., Avigad, D., Gerdes, A., 2014. Peri-Amazonian provenance of the Proto-
873 Pelagonian basement (Greece), from zircon U–Pb geochronology and Lu–Hf isotopic
874 geochemistry. Lithos 184-187, 379-392.

875

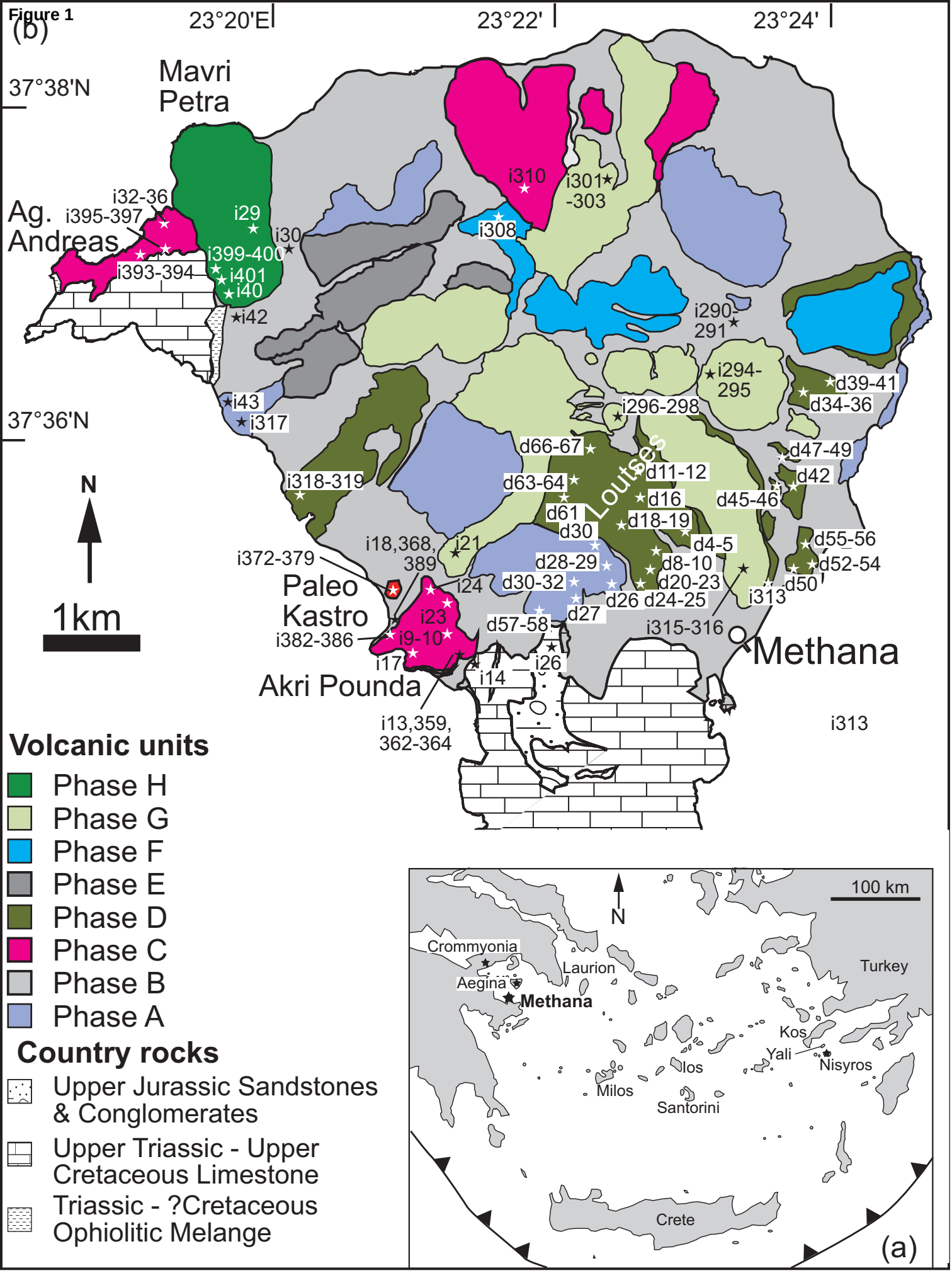

Fig. 1 Elburg et al.

Figure 2

Click here to download high resolution image

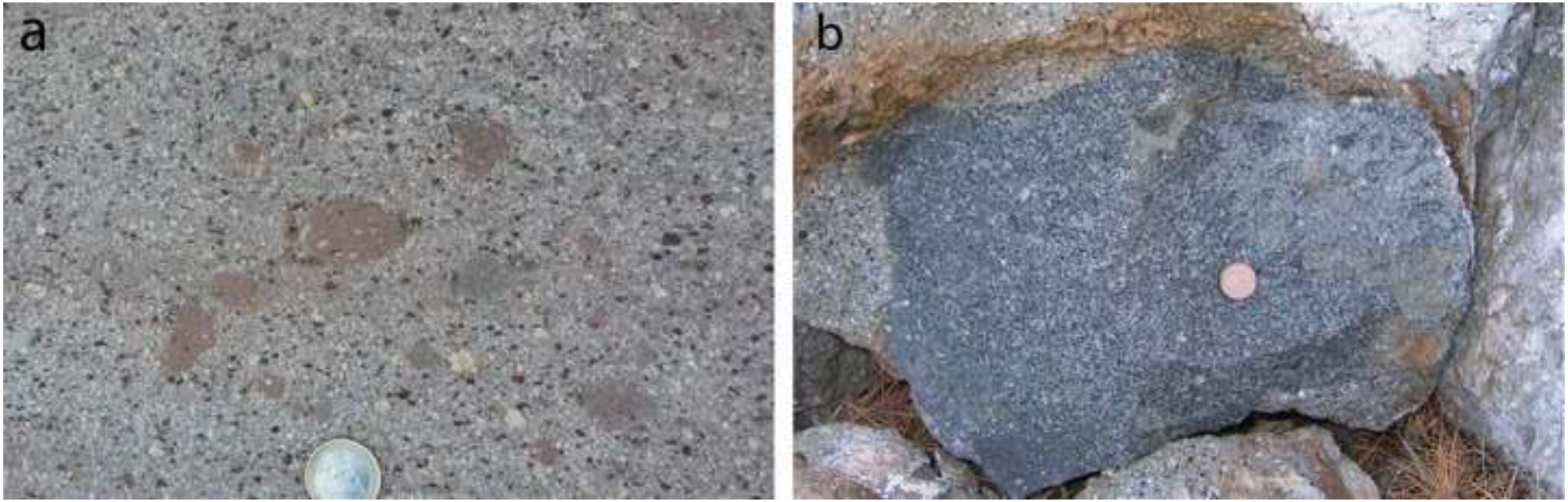

Figure 3

Click here to download high resolution image

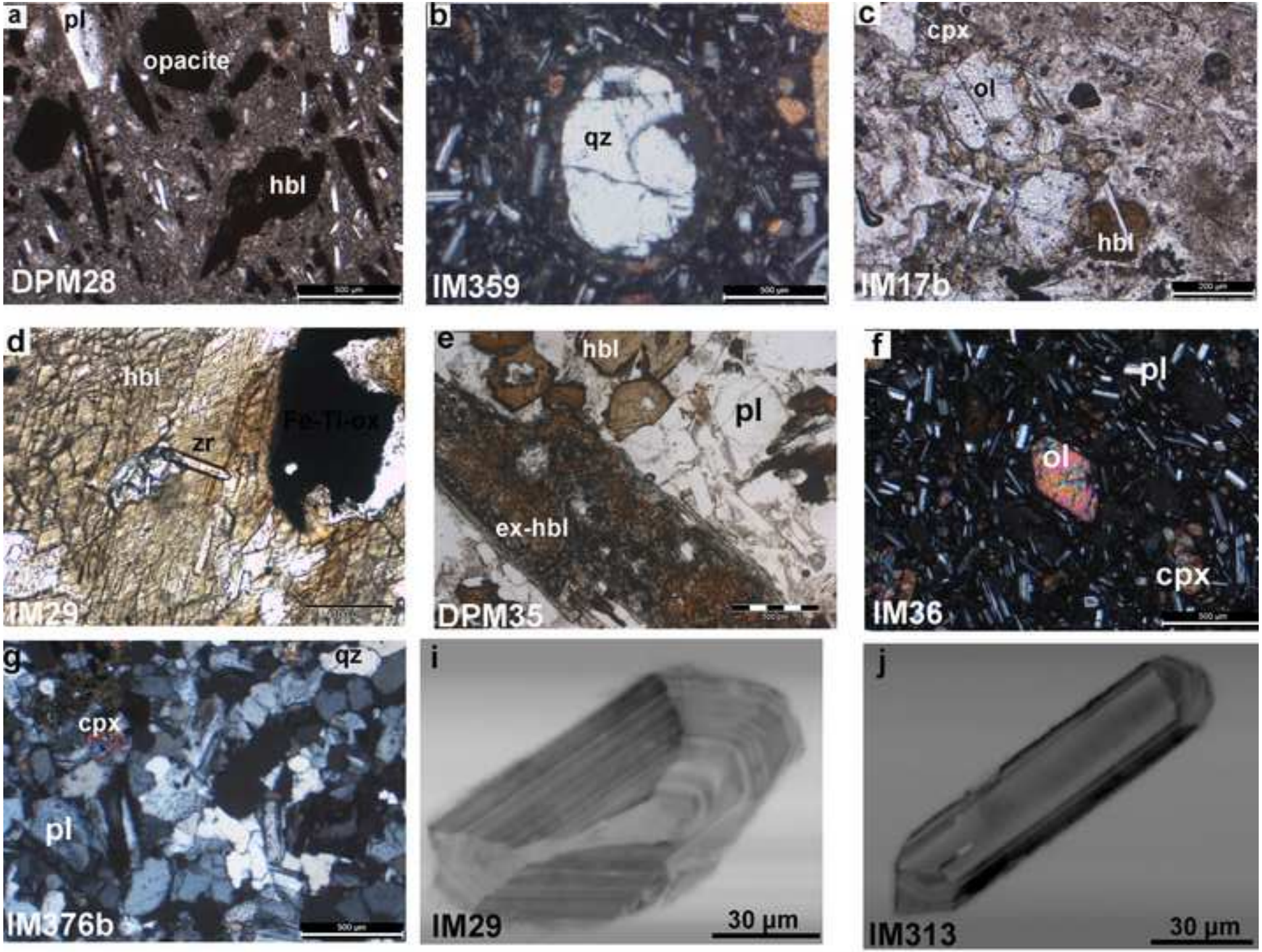

Figure 4

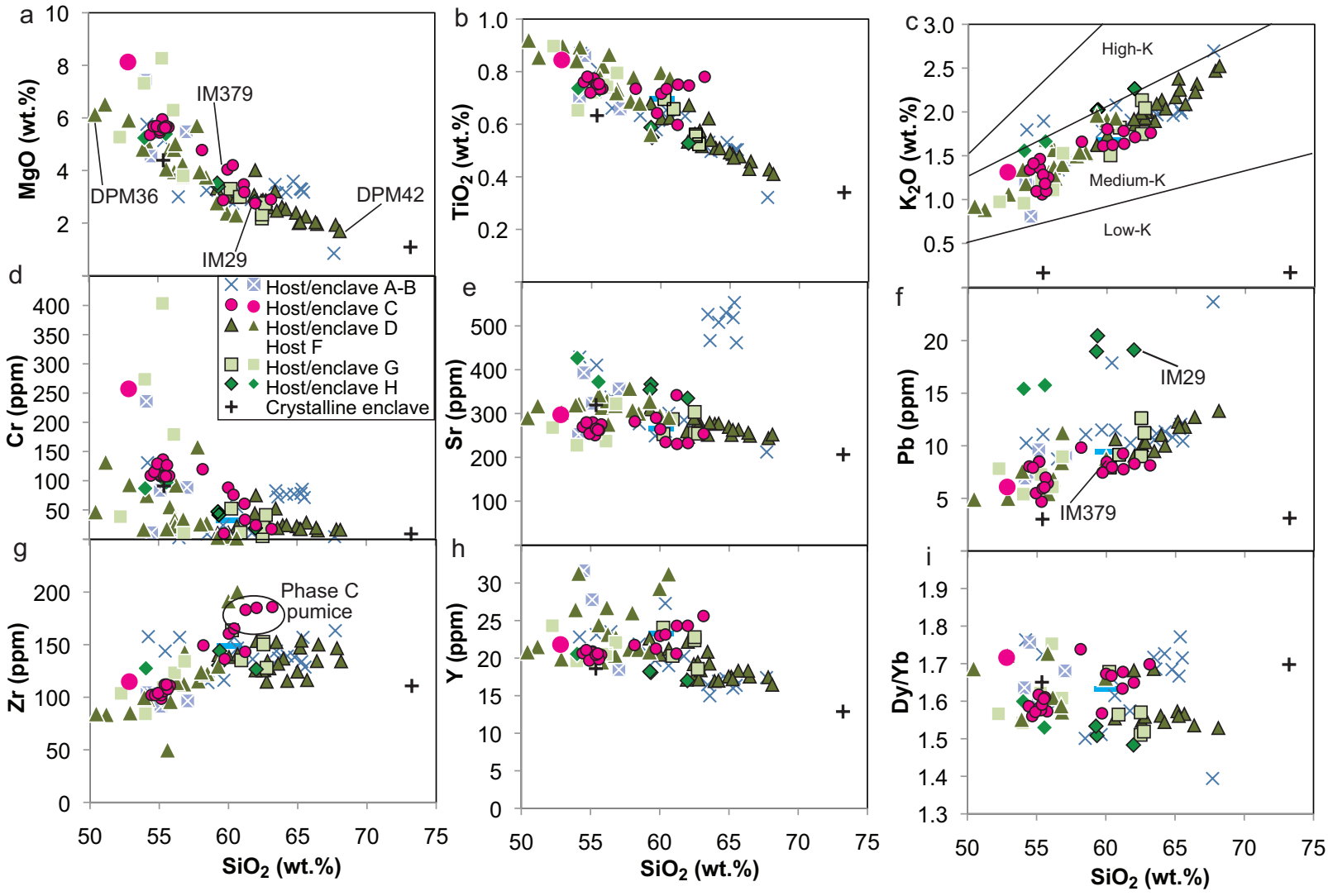

Fig. 4 Eburg et al.

Figure 5

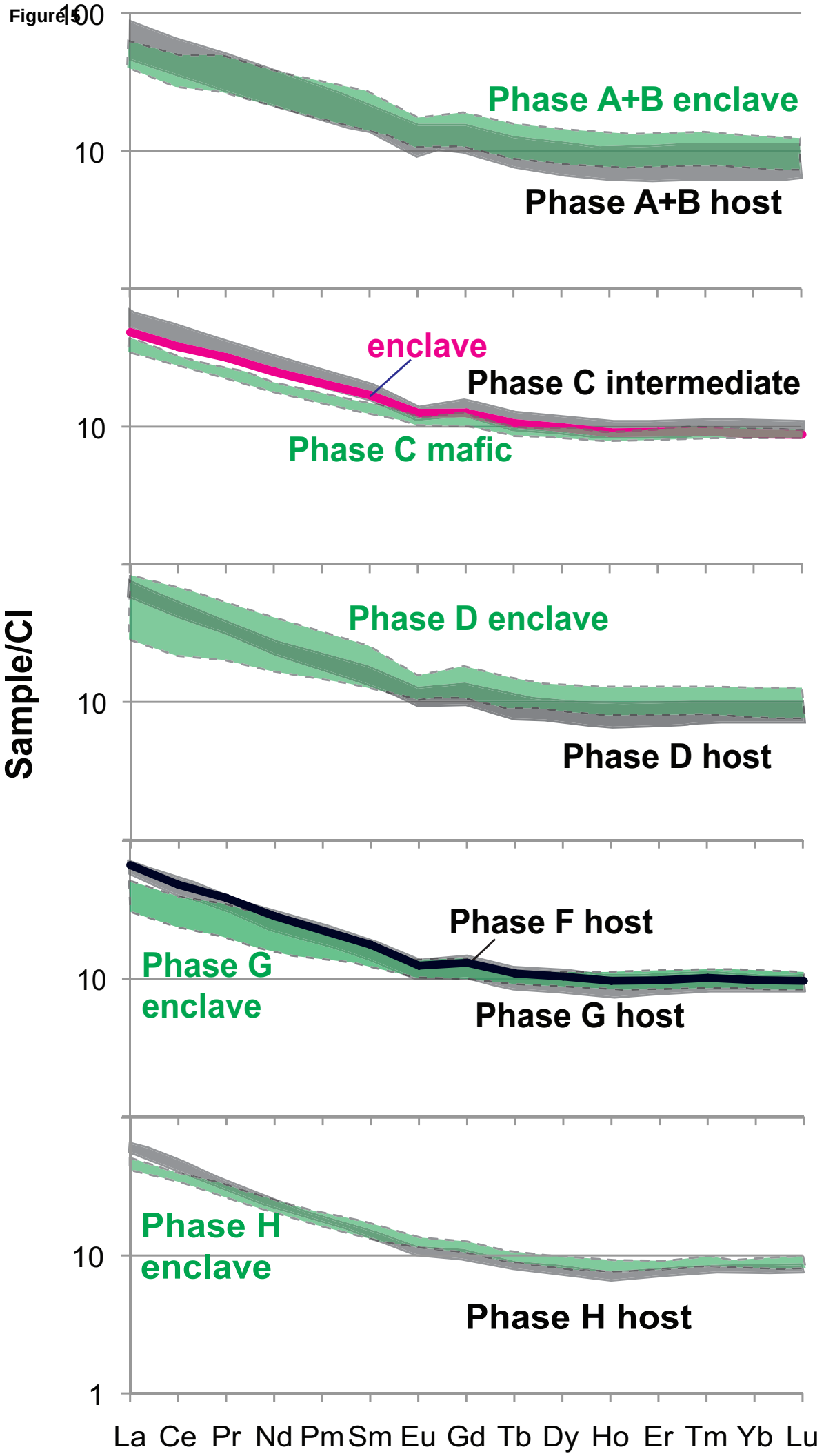
100
10
Phase A+B enclave
Phase A+B host
enclave
Phase C intermediate
10
Phase C mafic
Phase D enclave
10
Phase D host
Phase F host
Phase G
enclave
10
Phase G host
Phase H
enclave
10
Phase H host
1
Sample/CI
La Ce Pr Nd Pm Sm Eu Gd Tb Dy Ho Er Tm Yb Lu

Figure 6

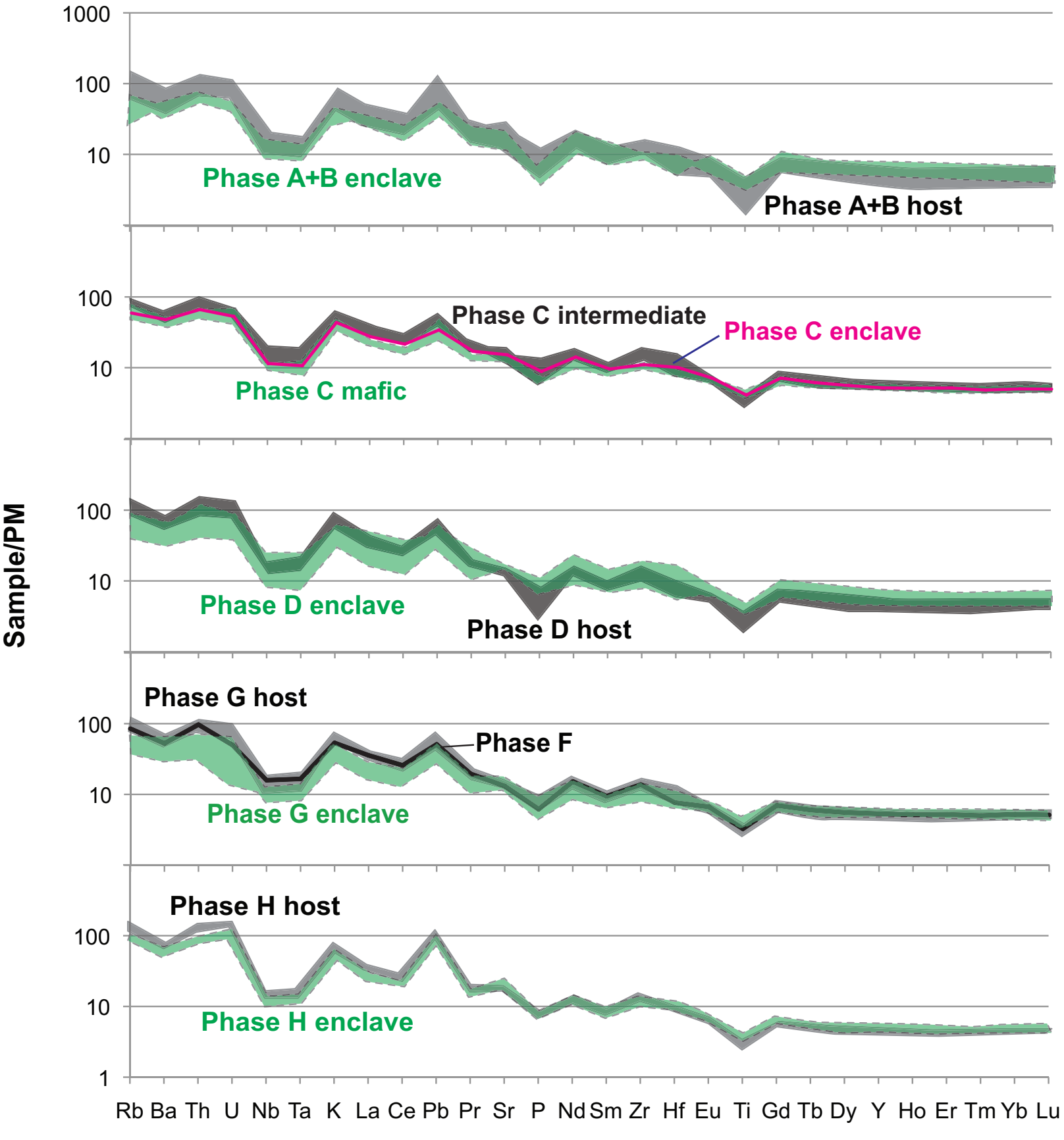
Sample/PM
1000
100
10
1
Phase A+B enclave
Phase A+B host
Phase C intermediate
Phase C enclave
Phase C mafic
Phase D enclave
Phase D host
Phase G host
Phase F
Phase G enclave
Phase H host
Phase H enclave
Rb Ba Th U Nb Ta K La Ce Pb Pr Sr P Nd Sm Zr Hf Eu Ti Gd Tb Dy Y Ho Er Tm Yb Lu

Figure 7

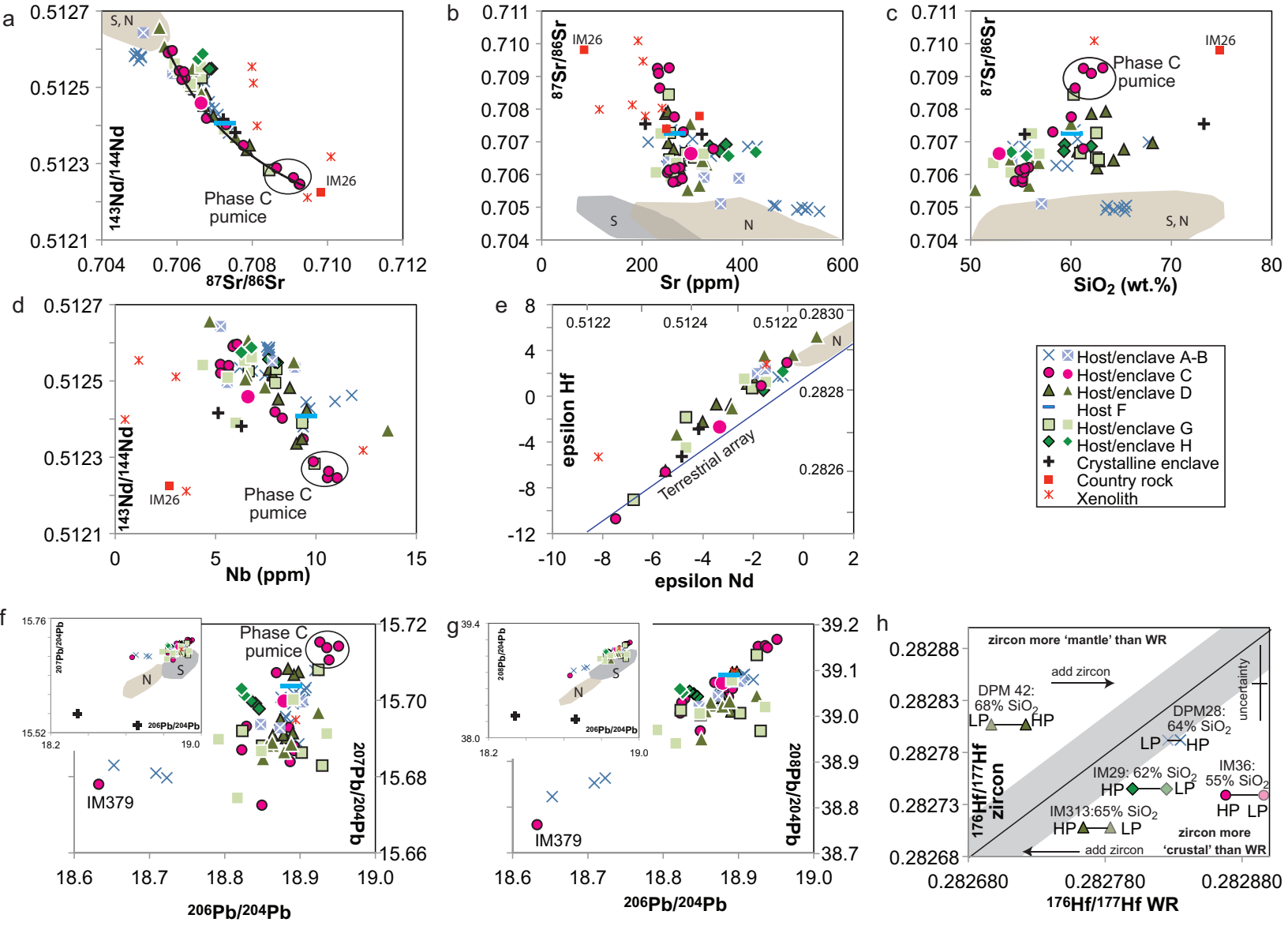
a
b
c
d
e
f
g
h
S, N
IM26
Phase C pumice
S
N
Host/enclave A-B
Host/enclave C
Host/enclave D
Host F
Host/enclave G
Host/enclave H
Crystalline enclave
Country rock
Xenolith
Terrestrial array
IM379
zircon more 'mantle' than WR
add zircon
DPM 42: 68% SiO2
DPM28: 64% SiO2
IM29: 62% SiO2
IM313:65% SiO2
IM36: 55% SiO2
uncertainty
zircon more 'crustal' than WR
LP
HP
87Sr/86Sr
143Nd/144Nd
Sr (ppm)
SiO2 (wt.%)
Nb (ppm)
epsilon Hf
epsilon Nd
206Pb/204Pb
207Pb/204Pb
208Pb/204Pb
176Hf/177Hf zircon
176Hf/177Hf WR

Figure 8

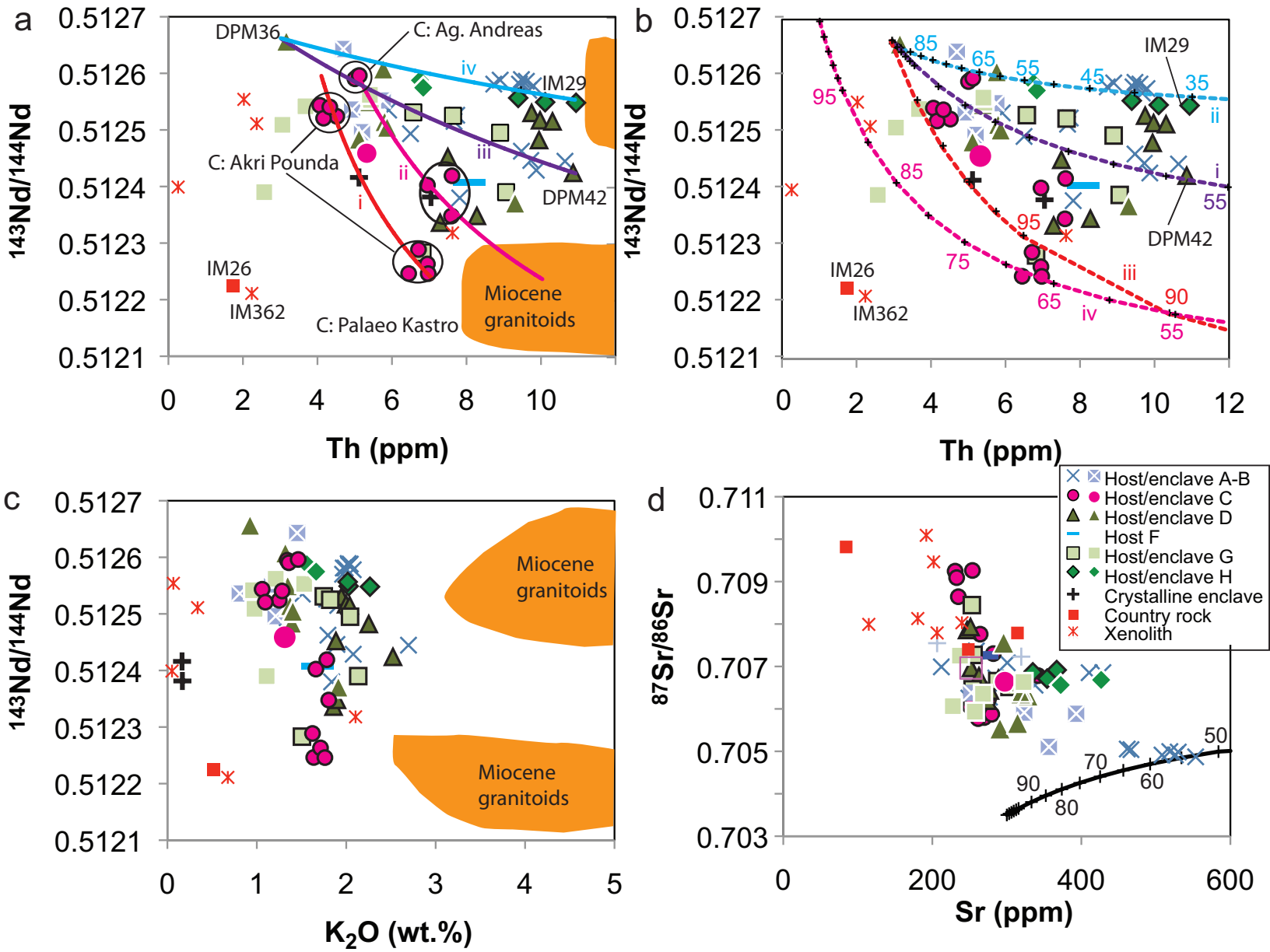

Fig. 8 Elburg et al.

Figure9

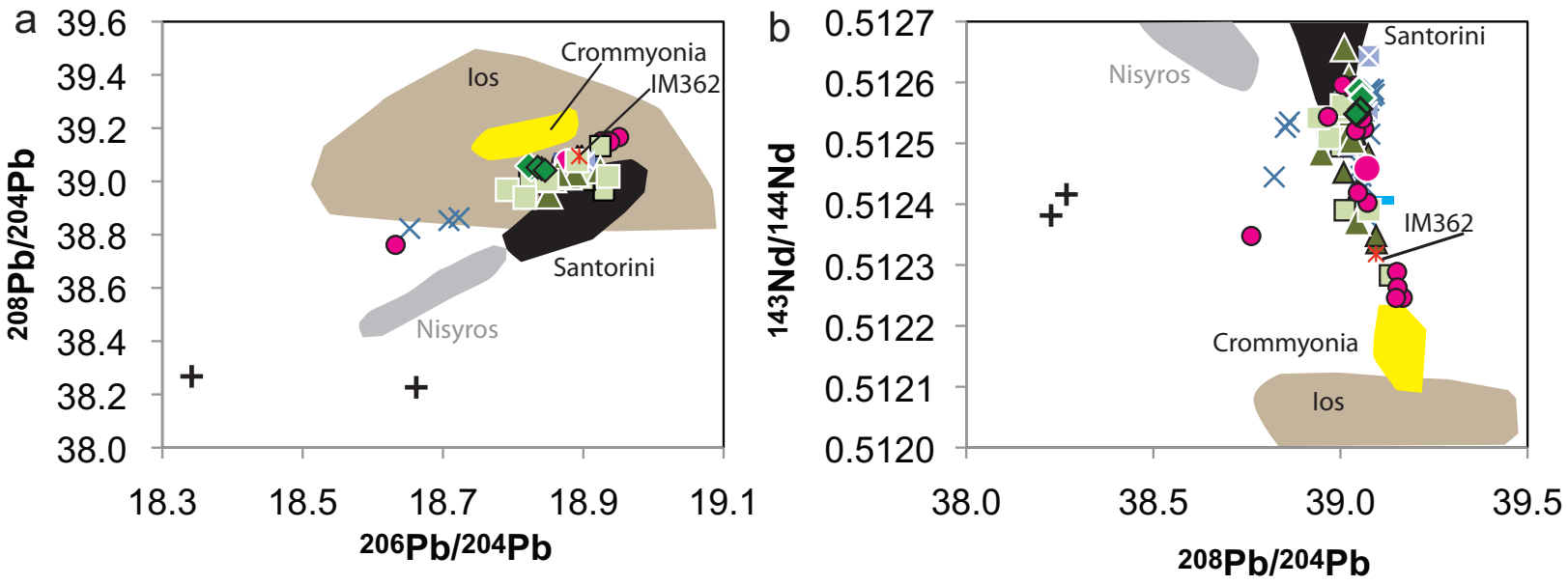

Fig. 9 Elburg et al.

Figure 10

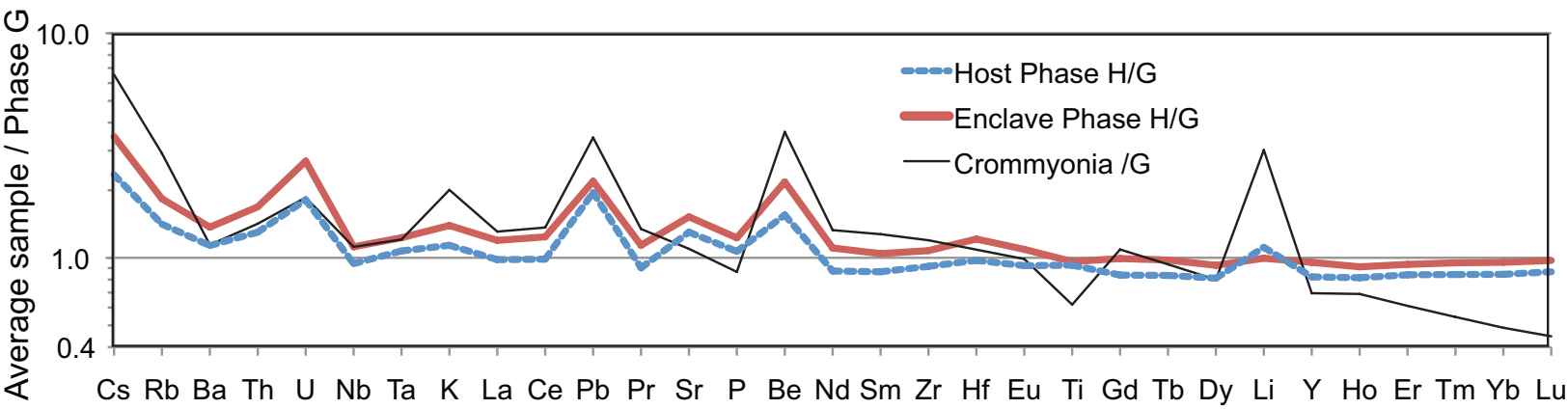

Fig. 10 Elburg et al.

Figure 11

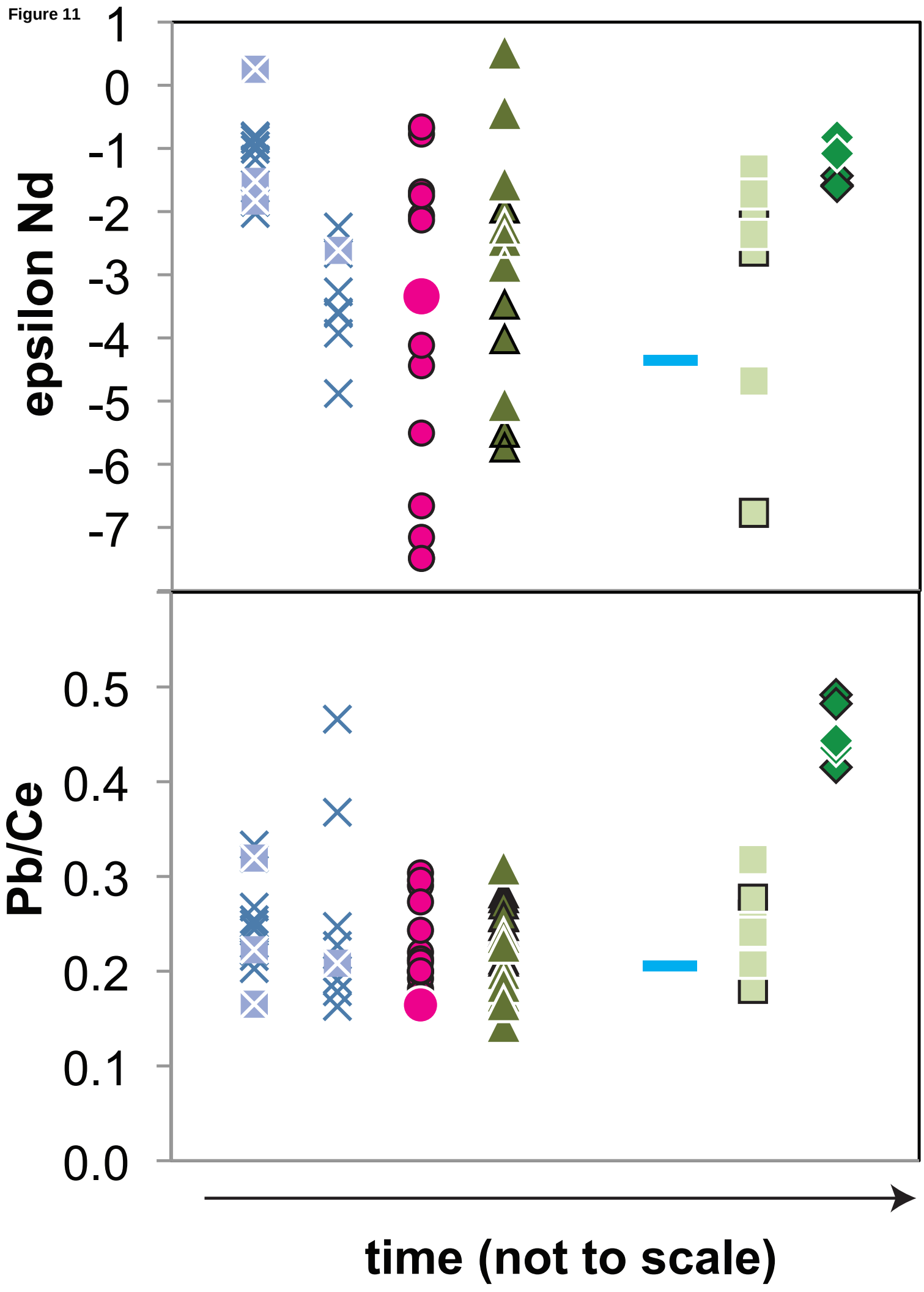

Figure 12

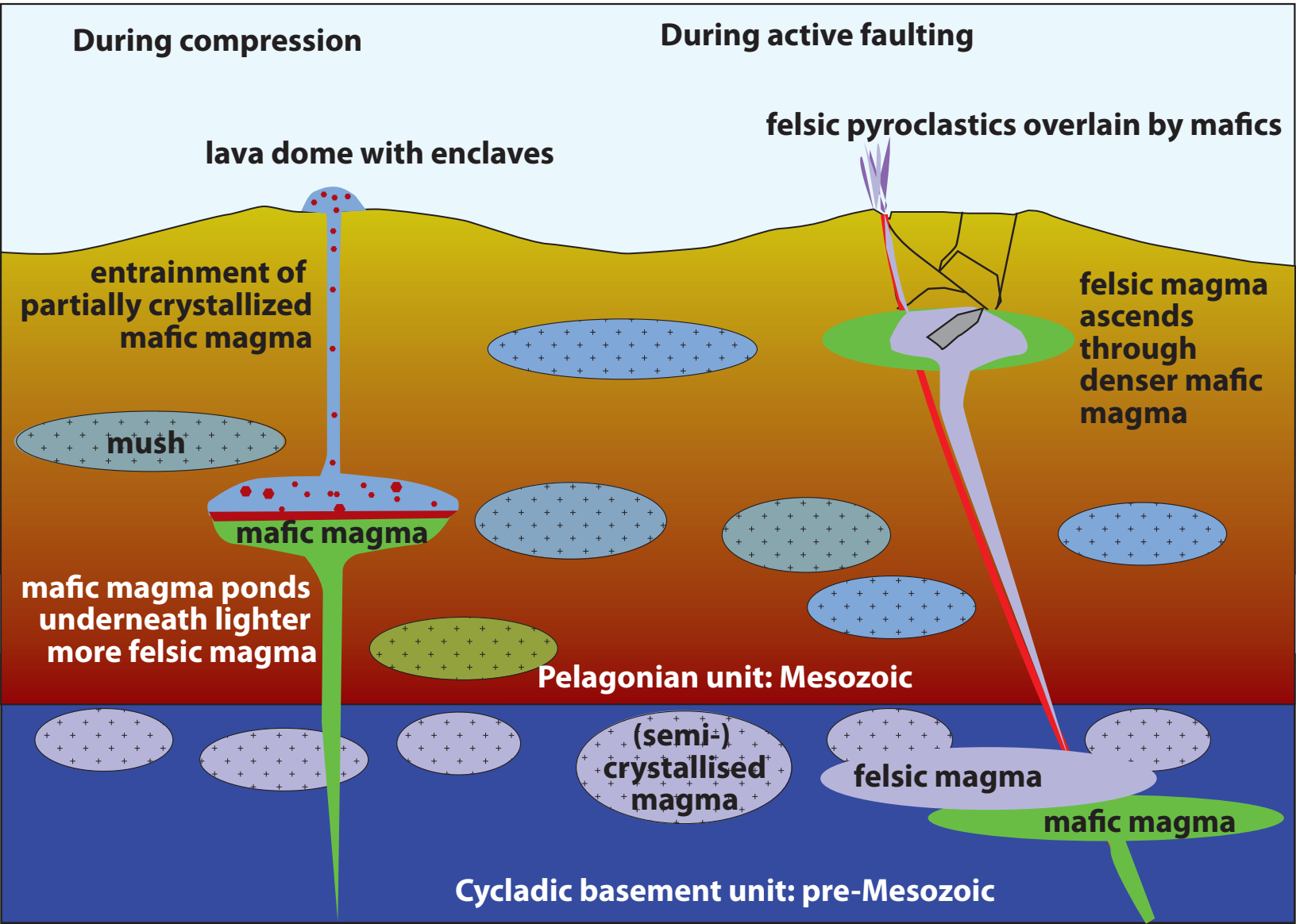
During compression
During active faulting
lava dome with enclaves
felsic pyroclastics overlain by mafics
entrainment of partially crystallized mafic magma
felsic magma ascends through denser mafic magma
mush
mafic magma
mafic magma ponds underneath lighter more felsic magma
Pelagonian unit: Mesozoic
(semi-) crystallised magma
felsic magma
mafic magma
Cycladic basement unit: pre-Mesozoic

Table 1

Click here to download Table: Table 1.docx

Table 1: Mixing end members for curves in Figures 7 and 8.

	Curve	$^{143}Nd/^{144}Nd$	Nd (ppm)	Th	$^{87}Sr/^{86}Sr$	Sr (ppm)	R
Phase C mixing	Fig. 7a						
primitive		0.51265	12		0.7055	300	
evolved		0.51224	22		0.7093	250	
	Fig. 8a i						
primitive		0.5126	12	4			
evolved		0.5122	22	7			
	Fig. 8a ii						
primitive		0.5126	12	5			
evolved		0.5122	22	10			
Phase D mixing	Fig. 8a iii						
primitive		0.51266	12	3			
evolved		0.51242	17	11			
Phase D mixing	Fig. 8a iv						
primitive		0.51266	12	3			
evolved		0.51255	16	11			
Phase D AFC	Fig. 8b i						
primitive		0.51266	12	3			
assimilant		0.51222	6	2			0.8
Phase H AFC	Fig. 8b ii						
primitive		0.51266	12	3			
assimilant		0.51222	6	2			0.4
Phase C AFC	Fig. 8b iii						
primitive		0.51266	12	3			
assimilant		0.5119	48	15			0.8
Phase C AFC	Fig. 8b iv						
primitive 2		0.5127	9	1	0.7055	350	0.4
assimilant		0.5119	48	15	0.743	100	
Methana HP AFC							
primitive	Fig. 8d	0.5129	9		0.7035	300	0.3
assimilant		0.5122	30		0.725	100	

Bulk distribution coefficients were taken as 0.3 for Nd, 0.001 for Th and 1.7 for Sr except for the high pressure (HP) model, where it was 0.1. R = ratio assimilation / fractionation (for AFC models).